EUMETSAT Satellite Application Facility on Climate Monitoring

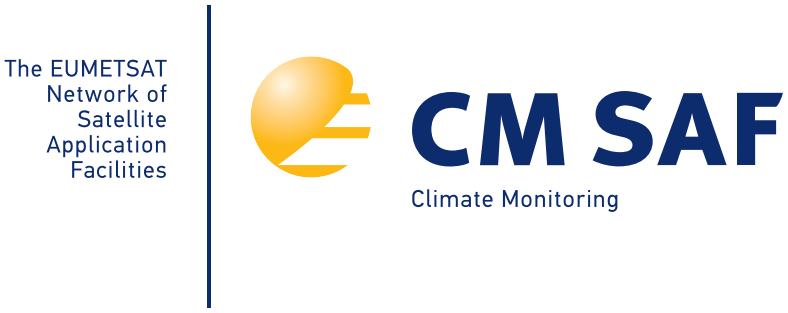

Algorithm Theoretical Basis Document

Meteosat Cloud Fractional Cover (COMET) Edition 1

DOI: 10.5676/EUM_SAF_CM/CFC_METEOSAT/V001

Cloud Fractional Cover **CM-23011**

Doc.No.: SAF/CM/MeteoSwiss/ATBD/MET/CFC
Issue: 1.3
Date: April 25, 2019

Document Signature Table

	Name	Function	Signature	Date
Authors	Reto Stöckli, Anke Duguay-Tetzlaff Jedrzej Bojanowski	CM-SAF Scientists		20.09.2016
Editor	Rainer Hollmann	Science Coordinator		09.05.2017
Approval	Steering Group			15.05.2017
Release	Martin Werscheck	Project Manager		22.08.2017

Distribution List

Internal Distribution	
Name	**No. Copies**
DWD Archive	1
CM SAF Team	1

External Distribution		
Company	**Name**	**No. Copies**
Public		1

Document Change Record

Issue Revision	Date	DCN no.	Changed pages / Paragraphs
1.0	10.08.2015	SAF/CM/MeteoSwiss/ATBD/MET/CFC	First version for PCR 2.8
1.1	02.11.2015	SAF/CM/MeteoSwiss/ATBD/MET/CFC	Revised version based on PCR 2.8 review requests
1.2	01.08.2016	SAF/CM/MeteoSwiss/ATBD/MET/CFC	Revised version for DRR 2.8
1.3	23.04.2019	SAF/CM/MeteoSwiss/ATBD/MET/CFC	Removed STT Score documentation since it was never used in the COMET code

Applicable Documents

Reference	Title	Code
AD 1	CM SAF Product Requirements Document	SAF/CM/DWD/PRD/2.7

Reference Documents

Reference	Title	Code
RD 1	Algorithm Theoretical Basis Document Meteosat Land Surface Temperature Edition 1	SAF/CM/MeteoSwiss/ATBD/MET/LST/1
RD 2	Algorithm Theoretical Basis Document Meteosat Free Tropospheric Humidity Edition 2	SAF/CM/DWD/ATBD/MET/FTH/2
RD 3	Validation Report Meteosat Meteosat Cloud Fractional Cover	SAF/CM/MeteoSwiss/VAL/MET/CFC/1
RD 4	Product User Manual Meteosat Meteosat Cloud Fractional Cover	SAF/CM/MeteoSwiss/PUM/MET/CFC/1

Contents

1 The EUMETSAT Satellite Application Facility on Climate Monitoring 10

2 Introduction 11

2.1 Overview . . . 11

2.2 Implementation . . . 11

2.3 Cloud Mask . . . 14

2.4 Cloud Fractional Cover . . . 15

3 Pre-Processing 16

3.1 Inter-Calibration . . . 16

3.1.1 MFG . . . 16

3.1.2 MSG . . . 18

3.2 Radiances . . . 18

3.3 Reflectances . . . 19

3.4 Brightness Temperatures . . . 19

3.4.1 MFG . . . 19

3.4.2 MSG . . . 19

3.5 Simulating the Broad Band VIS Channel . . . 20

4 Cloud Mask 20

4.1 Cloud Mask Scores . . . 21

4.1.1 Temperature Score . . . 21

4.1.2 Brightness Score . . . 21

4.1.3 Spatio-Temporal Reflectance Variance Score . . . 22

4.1.4 Temporal Temperature Variance Score . . . 22

4.2 Day-Night Separation . . . 23
4.3 Day-Night Regression . . . 23
4.4 Snow Detection . . . 23
4.5 Cloud Mask Classification . . . 23
4.6 Cloud Mask Uncertainty . . . 24
4.7 Cloud Top Height . . . 25
4.8 Cloud Top Pressure . . . 25

5 Clear Sky Compositing 26

5.1 Clear Sky Brightness Temperature . . . 26
5.1.1 Mannstein Model . . . 28
5.1.2 Göttsche Model . . . 30
5.2 Clear Sky Reflectance . . . 33

6 Cloud Fraction 38

6.1 Bayes Theorem in Cloud Detection . . . 38
6.2 Implementation . . . 39
6.3 Observational Constraint . . . 40
6.4 Conditional Probabilities . . . 42
6.5 Calculation of CA and CFC . . . 44
6.6 Evaluation of CA and CFC . . . 46
6.6.1 Instantaneous Skill Scores . . . 46
6.6.2 Daily and Monthly Mean Accuracy . . . 49

7 Spatial and Temporal Aggregation 51

8 Directions for Future Improvements 51

8.1 General . . . 51

8.2 Detailed . . . 52

9 Glossary **54**

10 References **56**

A Sensor Parameters **60**

A.1 Spectral Response Function . . . 60

A.2 Central Wavelength . . . 60

A.3 Bandwidth . . . 60

A.4 Spectral Solar Irradiance . . . 61

B Time **61**

C Angles **62**

C.1 Sun Angles . . . 62

C.2 Satellite Angles . . . 63

C.3 Sun-Satellite Angles . . . 66

C.4 Terrain Angles . . . 67

D Variability **68**

D.1 Spatial Variability . . . 68

D.2 Temporal Variability . . . 68

D.3 De-trended Temporal Variability . . . 69

D.4 Spatio-Temporal Variability . . . 69

E Boundary Conditions **69**

E.1 Elevation . . . 69

E.2 Land-Water Mask 69

E.3 Re-Analysis Data 70

F Geographic Projections **70**

F.1 Meteosat First Generation (forward) 70

F.2 Meteosat First Generation (inverse) 70

F.3 Meteosat Second Generation (forward) 70

F.4 Meteosat Second Generation (inverse) 70

F.5 Swiss Orthographic (forward) 70

F.6 Swiss Orthographic (inverse) 71

F.7 MODIS Sinusoidal (forward) 71

F.8 MODIS Sinusoidal (inverse) 71

F.9 Orthographic (forward) 72

F.10 Orthographic (inverse) 72

F.11 Rotated Pole (forward) 73

F.12 Rotated Pole (inverse) 73

F.13 Re-Projection 74

G Skill Scores **74**

G.1 Binary Skill Scores 74

G.2 Continuous Validation Scores 75

G.3 The Standard Normal Homogeneity Test 75

List of Figures

1 Schematic flowchart for the cloud mask and ECV processing of GeoSatClim 12

2 Three generations of cloud masking methods: classification based on a binary decision tree (left), classification using aggregated rating of continuous scores (center) and bayesian classification using cloud probability distributions (right). 14

3 Daily MFG MVIRI inter-calibration factors scale (left) and offset (right) for the WV (top) and IR (bottom) channel during 2005. Black circles are quality-screened daily inter-calibration factors from EUMETSAT; the red dotted line applies gaussian smoothing; the green dashed line applies weighted gaussian smoothing; the blue solid line applies break detection followed by weighted gaussian smoothing. 17

4 Meteosat 7 MVIRI versus MSG1 SEVIRI ToA brightness temperatures for the WV (left) and IR (right) channel covering the whole year of 2005 and for the pixel closest to WMO station Payerne (WMO ID 06610). Black circles: using original MFG radiances. Red circles: using inter-calibrated MFG radiances. 18

5 Examples of the diurnal temperature model after Mannstein et al. (1999) at four sites given in Table 3. Meteosat all sky (orange crosses), cloud masked (blue circles including cloud mask uncertainty) and corresponding modeled clear sky (pink filled circles) ToA brightness temperature. 29

6 Examples of the diurnal temperature model after Göttsche and Olesen (2009) at four sites given in Table 3. Meteosat all sky (orange crosses), cloud masked (blue circles including cloud mask uncertainty) and corresponding modeled clear sky (pink filled circles) ToA brightness temperature. 32

7 Examples of the diurnal clear sky reflectance model using only 3 parameters at four sites given in Table 3. Meteosat all sky (orange crosses), cloud masked (blue circles including cloud mask uncertainty) and corresponding modeled clear sky (pink filled circles) ToA reflectance. 36

8 Examples of the diurnal clear sky reflectance model using all 7 parameters at four sites given in Table 3. Meteosat all sky (orange crosses), cloud masked (blue circles including cloud mask uncertainty) and corresponding modeled clear sky (pink filled circles) ToA reflectance. 37

9 Prior probability of cloud occurrence on the Meteosat Disc binned by cloud amount (CA) class. 41

10 Left: all quality screened SYNOP reporting WMO sites. Right: same as left, but gridded to a 2° x 2° geographic grid. 42

11 Conditional probability of cloud occurrence in dependence of the Brightness Score $\mathrm{B}_{\mathrm{score}}$ and the Spatio-Temporal Reflectance Variance Score $\mathrm{STR}_{\mathrm{score}}$ on the Meteosat Disc for cloud amount (CA) classes 1, 3, 5 and 7. Conditional proabilities add up to unity for each CA class. 43

12 Conditional probability of cloud occurrence in dependence of both the Temperature Score $\mathrm{T}_{\mathrm{score}}$ and the Temporal Temperature Variance Score $\mathrm{TV}_{\mathrm{score}}$ on the Meteosat Disc for cloud amount (CA) classes 1, 3, 5 and 7. 45

13 Instantaneous binary skill score statistics of the MFG MVIRI-based CA during 2005 based on 565 SYNOP sites: Hansen-Kuiper's skill score (HK) vs. sun and satellite view zenith angle (upper left and right) and bias score vs. sun and satellite view zenith angle (lower left and right). 47

14 Instantaneous binary skill score statistics of the MSG SEVIRI-based CA during 2005 based on 556 SYNOP sites: Hansen-Kuiper's skill score (HK) vs. sun and satellite view zenith angle (upper left and right) and bias score vs. sun and satellite view zenith angle (lower left and right). 48

15 Hourly (left) and monthly (right) continuous statistics of the MFG MVIRI-based CFC during 2005 based on 565 SYNOP sites. 49

16 Hourly (left) and monthly (right) continuous statistics of the MSG SEVIRI-based CFC during 2005 based on 556 SYNOP sites. 49

List of Tables

1 Offset and scale factors for each of the cloud mask scores. These factors are valid for the MVIRI and SEVIRI sensor and might need to be adjusted for other sensors. . . . 21

2 Parameters of the Mannstein et al. (1999) model 28

3 Geographic locations of the sites used for the clear sky brightness temperature and reflectance model examples. Elevation is given as elevation above sea level and is the mean Meteosat pixel altitude (and not the exact site altitude). 28

4 Parameters of the Göttsche and Olesen (2009) model 31

5 Parameters of the clear sky reflectance model 35

6 The two dimensional feature histograms selected for the Bayesian classifier. 40

7 Relationship of cloud amount (CA) to cloud fractional cover (CFC). 44

9 Reference to the documents containing sensor-specific spectral response functions . 60

10 Empirical coefficients needed to calculate the equation of time and declination 63

1 The EUMETSAT Satellite Application Facility on Climate Monitoring

The importance of climate monitoring with satellites was recognized in 2000 by EUMETSAT Member States when they amended the EUMETSAT Convention to affirm that the EUMETSAT mandate is also to contribute to the operational monitoring of the climate and the detection of global climatic changes". Following this, EUMETSAT established within its Satellite Application Facility (SAF) network a dedicated centre, the SAF on Climate Monitoring (CM SAF, http://www.cmsaf.eu).
The consortium of CM SAF currently comprises the Deutscher Wetterdienst (DWD) as host institute, and the partners from the Royal Meteorological Institute of Belgium (RMIB), the Finnish Meteorological Institute (FMI), the Royal Meteorological Institute of the Netherlands (KNMI), the Swedish Meteorological and Hydrological Institute (SMHI), the Swiss Federal Office of Meteorology and Climatology (MeteoSwiss), and the Meteorological Service of the United Kingdom (UK MetOffice). Since the beginning in 1999, the EUMETSAT Satellite Application Facility on Climate Monitoring (CM SAF) has developed and will continue to develop capabilities for a sustained generation and provision of Climate Data Records (CDRs) derived from operational meteorological satellites.
In particular the generation of long-term data sets is pursued. The ultimate aim is to make the resulting data sets suitable for the analysis of climate variability and potentially the detection of climate trends. CM SAF works in close collaboration with the EUMETSAT Central Facility and liaises with other satellite operators to advance the availability, quality and usability of Fundamental Climate Data Records (FCDR's) as defined by the Global Climate Observing System (GCOS). As a major task the CM SAF utilizes FCDR's to produce records of Essential Climate Variables (ECV's) as defined by GCOS. Thematically, the focus of CM SAF is on ECVs associated with the global energy and water cycle.
Another essential task of CM SAF is to produce data sets that can serve applications related to the new Global Framework of Climate Services initiated by the WMO World Climate Conference-3 in 2009. CM SAF is supporting climate services at national meteorological and hydrological services (NMHSs) with long-term data records but also with data sets produced close to real time that can be used to prepare monthly/annual updates of the state of the climate. Both types of products together allow for a consistent description of mean values, anomalies, variability and potential trends for the chosen ECVs. CM SAF ECV data sets also serve the improvement of climate models both at global and regional scale. As an essential partner in the related international frameworks, in particular WMO Sustained COordinated Processing of Environmental satellite data for Climate Monitoring (SCOPE-CM), the CM SAF - together with the EUMETSAT Central Facility, assumes the role as main implementer of EUMETSATs commitments in support to global climate monitoring. This is achieved through:

- Application of highest standards and guidelines as lined out by GCOS for the satellite data processing,
- Processing of satellite data within a true international collaboration benefiting from developments at international level and pollinating the partnership with own ideas and standards,
- Intensive validation and improvement of the CM SAF climate data records,
- Taking a major role in data set assessments performed by research organisations such as WCRP (World Climate Research Program). This role provides the CM SAF with deep contacts to research organizations that form a substantial user group for the CM SAF CDRs,
- Maintaining and providing an operational and sustained infrastructure that can serve the com-

munity within the transition of mature CDR products from the research community into operational environments.

A catalogue of all available CM SAF products is accessible via the CM SAF webpage, http://www.cmsaf.eu. Here, detailed information about product ordering, add-on tools, sample programs and documentation is provided.

2 Introduction

2.1 Overview

This CM SAF Algorithm Theoretical Basis Document (ATBD) provides information on the retrieval algorithms implemented to calculate the Meteosat Cloud Fractional Cover (CFC) Thematic Climate Data Record (TCDR) from Meteosat First Generation (MFG) and Second Generation (MSG) heritage channels with the GeoSatClim processing package. GeoSatClim was developed at the Swiss Federal Office of Meteorology and Climatology MeteoSwiss (http://www.meteoswiss.admin.ch) as part of their engagement within CM SAF's second Continuous Development and Operations Phase (CDOP-2). The authors would like to express their thanks to Rebekka Posselt (MeteoSwiss) who started off with the technical and scientific implementation of GeoSatClim in CDOP-2 before the new team took over. Within CM SAF CDOP-2 GeoSatClim is also used for the retrieval of the downstream variables Land Surface Temperature (LST) and Free Tropospheric Humidity (FTH). The retrieval of these variables is documented in separate ATBD's (RD-1 and RD-2). GeoSatClim is currently implemented for the retrieval of Geostationary Surface Albedo (GSA) at EUMETSAT as part of the MeteoSwiss participation in the SCOPE-CM project SCM-03 [1]. The CM and CFC retrieval presented here may be further applied for the retrieval of other land surface, oceanic and atmospheric quantities and for other heritage geostationary sensors such as the Geostationary Operational Environmental Satellite (GOES) and the Geostationary Meteorological Satellite (GMS).

The performance of the Meteosat CFC TCDR is documented in the Validation Report [RD-3] and information on the TCDR technical parts and data formats is presented in the Product User Manual (RD-4].

2.2 Implementation

The Cloud Mask (CM) and Cloud Fractional Cover (CFC or Cloud Amount CA) retrieval are distinct and separate parts of GeoSatClim and serve different needs. The CM is needed to composite clear sky (cloud free) reflectance and brightness temperature diurnal cycles once per day taking into account new cloud masked (clear sky) measurements of the respective day. These diurnal cycles are then used as background information in the downstream Bayesian CFC calculation. As a difference to most satellite-based CFC estimations, the CM itself is not used for the CFC calculation. It is thus very important to understand both the cloud mask and the clear sky compositing in order to follow the CFC estimation later on.

[1] The source code of GeoSatClim can be accessed by registered members and its functionality can be extended by use of the high performance computing software exchange platform hpcforge.org

The CM, CFC retrieval rely on the availability of inter-calibrated radiances and make use of sensor-specific spectral response functions. The retrieval is carried out with the following steps illustrated in Figure 1:

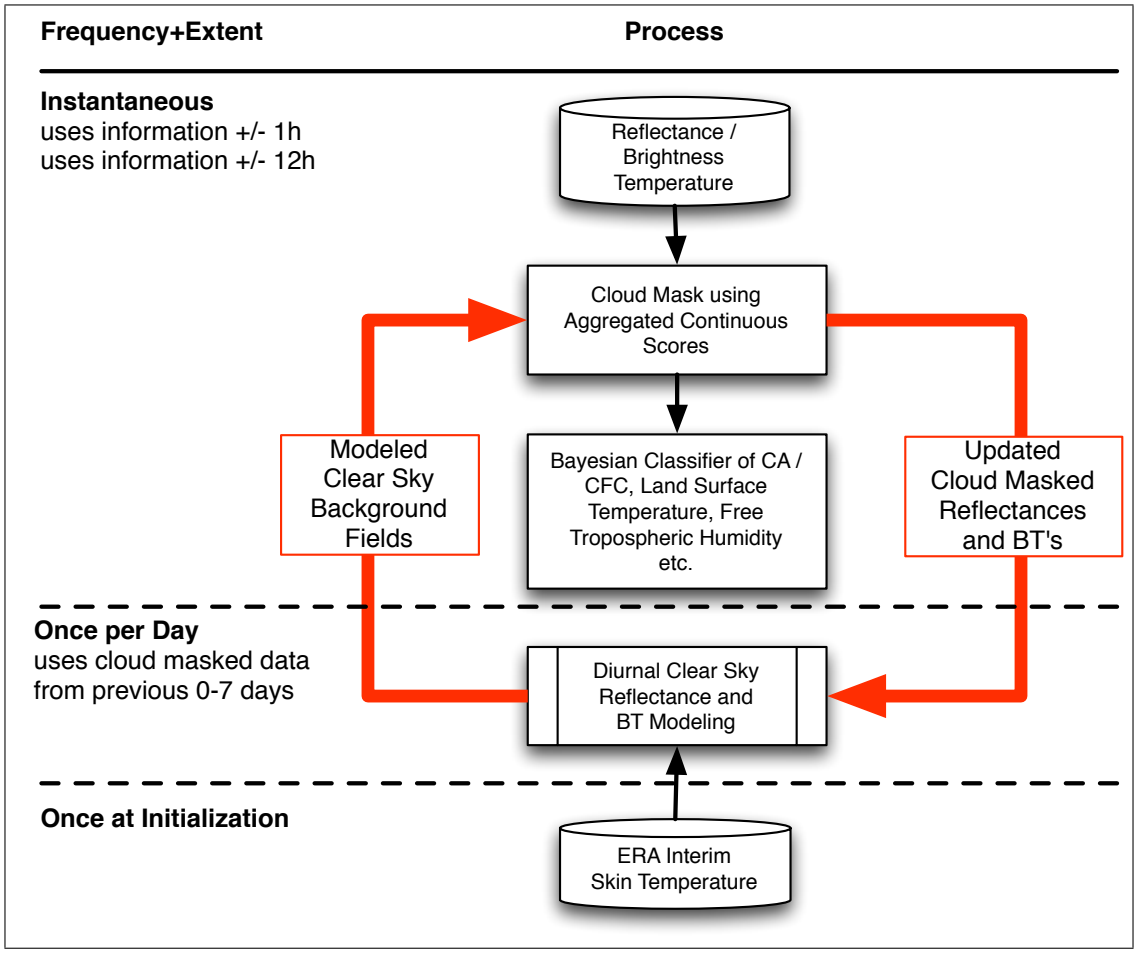

Figure 1: Schematic flowchart for the cloud mask and ECV processing of GeoSatClim .

1. Retrieve reflectances and brightness temperatures on native satellite grid.
2. Calculate preliminary cloud mask based on previous day's clear sky background fields.
3. Retrieve updated (this day's) clear sky background fields based on new cloud masked reflectances and brightness temperatures.
4. Calculate final cloud mask based on updated clear sky background fields.
5. Calculate downstream variables like CA, CFC, LST or FTH using cloudy or clear sky reflectances and brightness temperatures.
6. Spatially aggregate ECV's from native satellite grid to chosen geographical output projection (not shown).
7. Temporally aggregate ECV's from native satellite time resolution to hourly, daily and monthly time resolution (not shown).

The often chosen linear time slot by time slot cloud masking, clear sky compositing and successive retrieval of the physical state variables from the instantaneous reflectances and brightness temperatures and external background fields is replaced here with the following methodology:

- **Processing the Full Day:** In order to retrieve CM, CA and CFC always a full day of reflectances and brightness temperatures is read and analyzed. All processes in Figure 1 are carried out at once over 48 time slots of MFG MVIRI and 96 time slots of MSG SEVIRI. Due to the use of temporal variability (see below) the daily processing includes information from the previous and the next day. Such a strategy is restricted to climatological TCDR and Interim Climate Data Records (ICDR) processing and substantially differs from single time slot processing used in classical retrieval schemes.
- **Exploiting Spatio-Temporal Variability:** The cloud mask (upper part of Figure 1) includes temporal and spatial variability of ± 1 or also ± 12 hours as well as ± 2 pixel in addition to the instantaneous pixel states. Such a strategy is required in order to replace missing spectral information from heritage satellite sensors by maximizing the use of available information.
- **Diurnal Clear Sky Compositing:** The performance of a cloud mask highly depends on the realism of the assumed clear sky "background" reflectances and brightness temperatures (BT's). While most cloud masks rely on external sources for these background fields (such as NWP model-based surface temperature or climatological albedo composites), Geostationary satellite platforms with their high temporal coverage are actually suited to derive their own self-constrained and self-contained clear sky background fields. In GeoSatClim a daily recurring parametric estimation of clear sky background fields with diurnal cycle models of brightness temperature and reflectance constrained by previously cloud masked reflectances and brightness temperatures is implemented. This cyclic procedure is visualized by the red arrows in Figure 1. The estimated clear sky fields in turn improve successive cloud masking which are again the constraint for the next clear sky background field inversion. The self-contained estimation of clear sky field however is subject to the "chicken and egg" problem: NWP model-based skin temperature serves as "cold start" for the initial retrieval (lowest part of Figure 1). This diurnal clear sky compositing also requires a full day processing scheme and cannot be carried out with instantaneous retrievals. This cloud mask – clear sky compositing cycle is the most important part of the GeoSatClim . Compared to the use of external background fields the resulting clear sky fields represent the the actual satellite-observed state of surface (in both the spectral and spatial dimension). This is important for detecting clouds over rapidly changing surfaces such as snow cover, vegetation during green-up, floodplains, managed land cover or sea ice cover.

The full set of algorithms implemented as part of the GeoSatClim CM, CA and CFC retrieval as illustrated in Figure 1 is described in this report. The radiance, inter-calibration and reflectance and brightness temperature calculation are covered in Section 3. The CM retrieval is described in Section 4. The parametric diurnal clear sky inversion is described in Section 5. The Bayesian classifier used for the retrieval of CA and CFC is described in Section 6. The spatial and temporal aggregation of instantaneous retrievals is described in Section 7, followed by a few recommendations for improvements of the presented algorithms in Section 8. The Appendix contains a detailed scientific description of algorithms referred to from the main Sections.

2.3 Cloud Mask

The cloud mask of GeoSatClim is based on the methodology of additive continuous cloud scores, also termed “aggregated rating”. This methodology is part of the Separation of Pixels using an Aggregated Rating over Canada (SPARC) algorithm by Khlopenkov and Trishchenko (2007). SPARC has been developed to provide a cloud, cloud shadow and snow detection for the 5 channels of the polar orbiting Advanced Very High Resolution (AVHRR) sensor from the National Oceanic and Atmospheric Administration (NOAA). The idea has been applied to the Meteosat Second Generation SEVIRI and Meteosat First Generation MVIRI sensor data by using a newly developed set of scores with a different clear sky compositing (Fontana et al., 2010; Stöckli, 2013). The cloud mask uses a summation of continuous scores (A, B, C and D in the center panel of Figure 2). This allows to calculate the cloud mask even with a partial availability of the spectral cloud mask scores (D could for instance be missing). In comparison, most historical cloud masks such as the NWC SAF (Dybbroe et al., 2005), CLAVR (Vemury et al., 2001) or APOLLO (Kriebel et al., 2003) cloud masks use a classification tree in which every binary test depends on the successful execution of previous (upstream) tests (Test B depends on Test A in the left panel of Figure 2). They thus are not applicable across satellite sensors and satellite sensor generations where differing spectral coverage only enables the execution of a sensor-specific set of tests. Misclassification may further occur with binary classification trees since upstream tests influence the effectiveness of downstream tests. The left panel of Figure 2 exemplifies how Test B is never actually considered if Test A results into Bin 3. In comparison the final decision of the aggregated rating approach is only made once all (continuous and not binary) tests have been conducted. Test A can indicate cloud cover and Test B can indicate cloud free. The result is a CM with a fuzzy instead of a binary decision: the aggregated rating for such a case is likely “undecided”, or applied to cloud masking: partially cloudy.

The success of this aggregated rating method, when applied to heritage sensors with only two channels, depends on:

- using continuous scores which are independent of the clear sky background (i.e. build difference scores and continuously retrieve the clear sky background);
- make full utilization of spatio-temporal information of geostationary sensors (i.e. use temporal variance and spatial variance in scores).

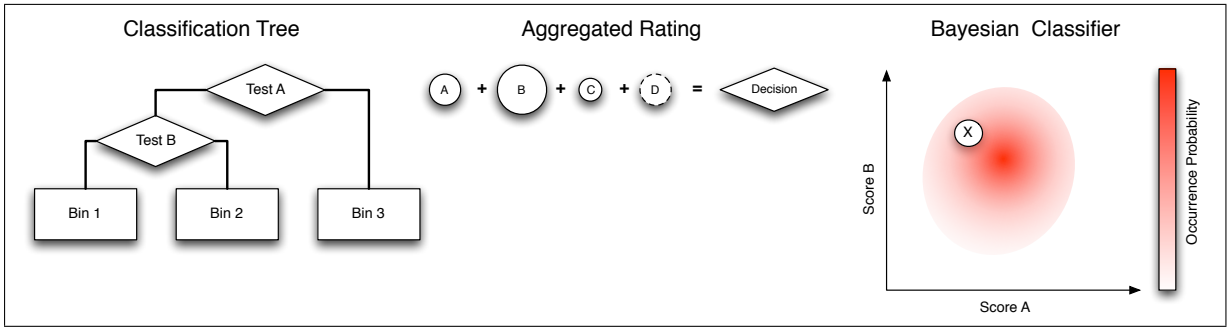

Figure 2: Three generations of cloud masking methods: classification based on a binary decision tree (left), classification using aggregated rating of continuous scores (center) and bayesian classification using cloud probability distributions (right).

2.4 Cloud Fractional Cover

A cloud mask is useful to generate an instantaneous cloud or clear sky conservative filter of clouds. This is needed to constrain downstream land surface or atmospheric TCDR's with reflectances or brightness temperatures which require to be fully cloud free or fully cloudy. It however is not suitable to represent the continuous state of cloudiness for climatological applications such as the monitoring of cloud cover variability and change. In order to calculate Cloud Amount (CA) or Cloud Fractional Cover (CFC) a Bayesian classifier has been implemented in GeoSatClim (right panel of Figure 2). It builds on the high number of synoptic cloud observations (SYNOP) available for the whole Meteosat period and covering the Meteosat Field of View (FoV). The continuous scores and the clear sky background fields of reflectance and brightness temperature are used together with the SYNOP data to calculate histograms of conditional occurrence probabilities for each CA and CFC class. As exemplified in the right panel of Figure 2 scores A and B can be calculated for each satellite observation X . The values of scores A and B are associated with a conditional occurrence probability for a discrete set of CA classes. The often applied naïve Bayesian classifiers (Heidinger et al., 2012; Hollstein et al., 2014; Karlsson et al., 2015) assume scores A and B to be independent (uncorrelated) and decisive predictors for cloud state. The Bayesian classifier implemented here explicitly exploits the co-variability of multiple scores. Figure 2 demonstrates how the occurrence probability of cloud state for satellite observation X can depend on both score A and score B. In GeoSatClim the probability of occurrence for a specific CA or CFC class is calculated from two dimensional joint probability histograms instead of using one-dimensional score-by-score probability histograms. The chosen strategy is a compromise between the requirements of implementing the full Bayesian classifier using N-dimensional histograms for N scores and the simplification made in the naïve Bayesian classifier.

3 Pre-Processing

3.1 Inter-Calibration

3.1.1 MFG

The MFG MVIRI VIS channel calibration factors are used as published by EUMETSAT (2010). It is based on a linear regression in time using calculated versus observed radiances over "stable" desert targets (Govaerts et al., 2004). It has been shown that the broad band VIS channel's decay is spectrally sensitive (with a more pronounced aging in the blue part of the spectrum). Novel spectral calibration methods have been developed and may be applied in the future for optimal accuracy (Decoster et al., 2013a, 2014). These models are however not yet suitable for TCDR processing since they require a dynamic and pixel-by-pixel estimation of spectral composition of the MVIRI VIS channel (e.g. white clouds vs. the cloud free blue ocean).

The MFG MVIRI WV and IR channel inter-calibration factors are provided by EUMETSAT (John et al., 2019). These inter-calibration factors are based on a daily inter-calibration of MFG MVIRI with the High Resolution Infrared Radiation Sounder (HIRS) instrument on board the National Oceanic and Atmospheric Administration (NOAA) polar orbiting platforms. The inter-calibration is carried out with the spectral response function (SRF) of the respective MVIRI sensor (see Section A). The inter-calibration scale and offset factors have MSG radiance units (mW m^{-2} sr^{-1} (cm^{-1})$^{-1}$). In order to convert them to the spectral-integrated MFG radiance units (W m^{-2} sr^{-1}) the following conversion is applied:

$$R_{\mathrm{MFG}} = \frac{\Delta\nu_0^a}{1000\mathrm{mWW}^{-1}} R_{\mathrm{MSG}}, \tag{1}$$

where $\Delta\nu_0^a$ is the actual channel bandwidth as a wavenumber (cm^{-1}) calculated from the SRF (see Section A) and the division by 1000 is needed to convert mW to W . The daily MFG MVIRI WV and IR channel inter-calibration factors are subject to spectral and spatio-temporal inter-calibration uncertainty and inter-calibration time-series can contain severe breaks due to MVIRI sensor gain changes (footprint, collocation and spectral differences, V. John, R. Roebeling and J. Schulz, personal communication). The following methods were applied to quality screen and "smooth" the factors in time before they are used to calculate inter-calibrated radiances:

1. remove inter-calibration factors with probability $q < 1$
2. weight inter-calibration factors with uncertainty $w = 1/\sigma$
3. detect break points in yearly time series
4. apply a piecewise gaussian smoothing between break points using 10 days half-with and weighted by w in order to smooth the "raw" values and fill gaps in time

Figure 3 demonstrates the effectiveness of the quality screening, break detection and smoothing: by use of a gaussian smoothing (red dotted lines) the day-to-day variability is removed. The weighting $w = 1/\sigma$ using the standard deviation σ of the daily inter-calibration linear fit dampens the sensitivity to outliers (green dashed lines). Continuous smoothing cannot be applied across sensor gain

changes, such as occurring for the scale factor of the WV channel. A detection of break points using based on known satellite changes and supported by the Standard Normal Homogeneity Test SNHT (Alexandersson, 1986; Haimberger, 2007) is applied prior to smoothing, followed by a piece-wise smoothing (blue solid lines). The SNHT window of ± 5 days is chosen and breaks are detected using a SNHT score above 100. For consecutive days with a score above 100 the day with the maximum score is selected as the break.

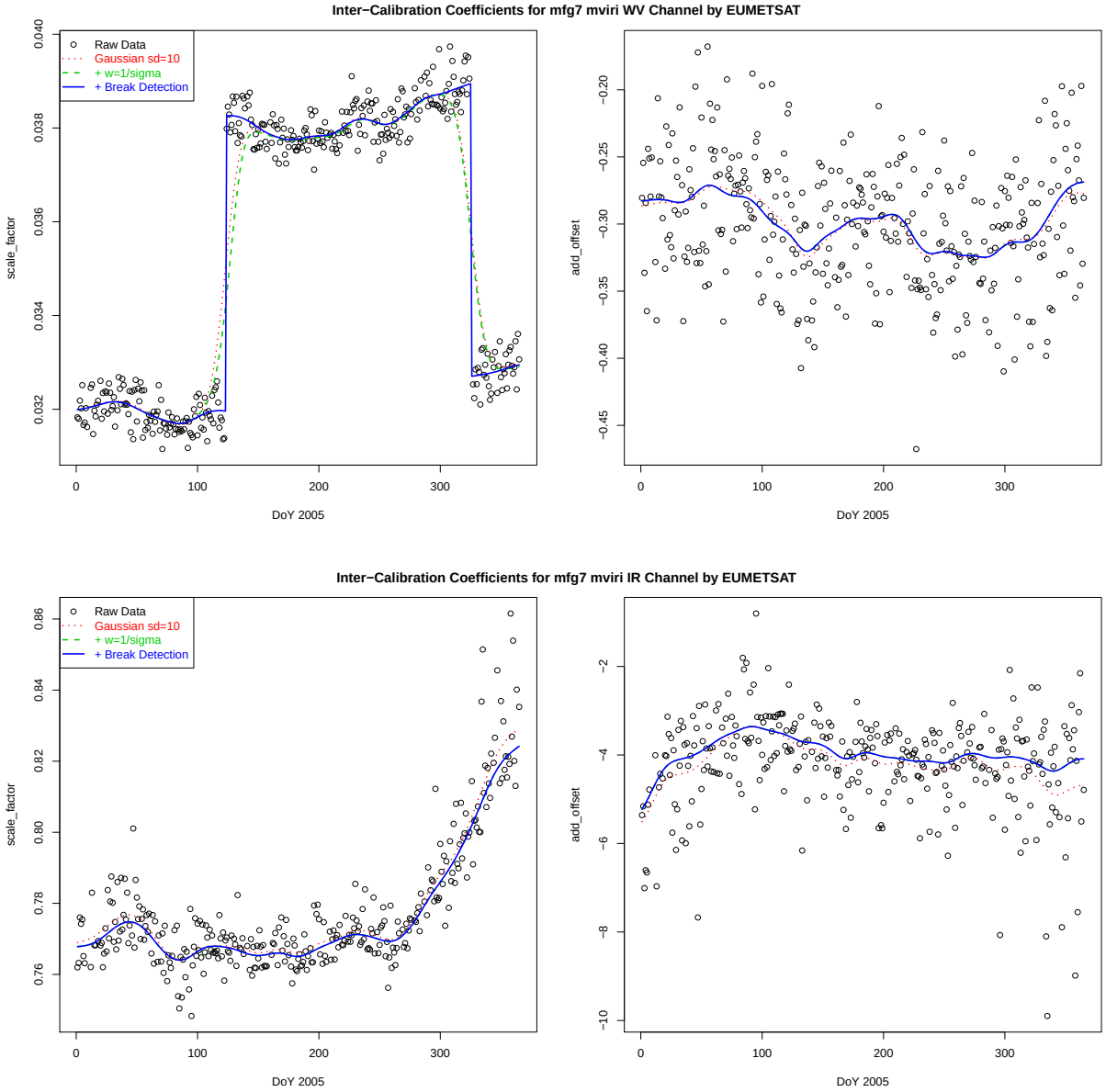

Figure 3: Daily MFG MVIRI inter-calibration factors scale (left) and offset (right) for the WV (top) and IR (bottom) channel during 2005. Black circles are quality-screened daily inter-calibration factors from EUMETSAT; the red dotted line applies gaussian smoothing; the green dashed line applies weighted gaussian smoothing; the blue solid line applies break detection followed by weighted gaussian smoothing.

Figure 4 shows that the use of the MFG inter-calibration decreases the mean bias error (MBE) between MFG MVIRI and MSG SEVIRI from -5.94 to -2.07 K for the WV channel and from 1.83 to 0.28

K for the IR channel. Much of the remaining MBE can be attributed to SRF differences. Especially for the WV channel these differences could be corrected when using Spectral Band Adjustment Factors (SBAF, V. John, R. Roebeling and J. Schulz, personal communication). The scatter on the other hand is mainly due to collocation differences between MFG and MSG.

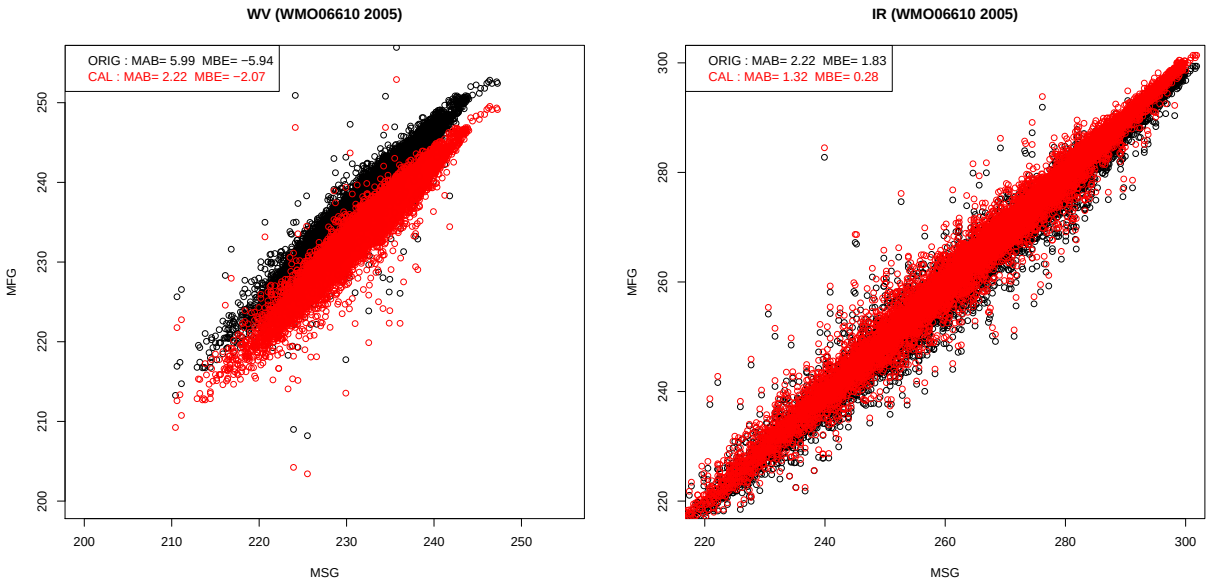

Figure 4: Meteosat 7 MVIRI versus MSG1 SEVIRI ToA brightness temperatures for the WV (left) and IR (right) channel covering the whole year of 2005 and for the pixel closest to WMO station Payerne (WMO ID 06610). Black circles: using original MFG radiances. Red circles: using inter-calibrated MFG radiances.

3.1.2 MSG

The original radiance calibration factors are used as provided as part of the Level 1.5 radiance data by EUMETSAT.

3.2 Radiances

The Meteosat Digital Numbers (DN) can be converted to ToA radiances. The native sensor specific radiance units are used: MFG MVIRI: W m^{-2} sr^{-1}; MSG SEVIRI: mW m^{-2} sr^{-1} (cm^{-1})$^{-1}$. The conversion employs the scale and offset calibration factors from the original Level 1.5 data or by using the inter-calibrated scale and offset values from the previous sub-section:

$$R = \text{scale} \cdot \text{DN} + \text{offset} \tag{2}$$

Radiance is only calculated if DN is higher than the so called "space count" $DC_0 = -\text{offset}/\text{scale}$. In GeoSatClim the MSG formulation with scale and offset is used to convert from DN to radiances.

For MFG the calibration factor C_f and the space count DC_0 is often used. They can be transformed to the MSG scale/offset formulation as follows:

$$\text{scale} = C_f \tag{3}$$
$$\text{offset} = -\text{scale} \cdot DC_0. \tag{4}$$

3.3 Reflectances

ToA reflectances are calculated by dividing the ToA radiances with the total band-integrated solar irradiance (TSI) R_s (radiance units, see Section 3.2 and Appendix A), normalized by the cosine of the sun zenith angle θ_s (see Appendix C) and the astronomical sun-earth distance d_s (AU) (see Appendix C):

$$\rho_x = \frac{R_x \pi d_\text{s}^2}{R_\text{s} \cos(\theta_\text{s})}, \tag{5}$$

where R_x are the MSG SEVIRI 0.6, 0.8 μm channel or the MFG MVIRI broad band VIS channel reflectances. Reflectance is only calculated for $\theta_\text{s} < 88°$.

3.4 Brightness Temperatures

3.4.1 MFG

ToA brightness temperature from MFG MVIRI are empirically related to the spectral radiance at each infrared channel (EUMETSAT, 2005):

$$T_x = \frac{\beta_x}{\ln(R_x) - \alpha_x}, \tag{6}$$

where x = WV or IR is one of the MFG MVIRI Infrared channels and R_x is the channel spectral radiance (W m^{-2} sr^{-1}). The regression coefficients α_x (-) and β_x (K) are defined by sensor (EUMETSAT, 2005).

3.4.2 MSG

A parametric expression with linear regression coefficients is used to convert the effective radiances of MSG SEVIRI to equivalent brightness temperatures (EUMETSAT, 2012):

$$T_x = \left(\frac{c_2 \nu_x}{\ln\left[1 + c_1 \nu_x^3 / R_x\right]} - \beta_x \right) / \alpha_x, \text{ where } \nu_x = \frac{10^4}{\lambda_x}, \tag{7}$$

where $x = 6.2$ or 10.8 μm is one of the MSG SEVIRI Infrared channels, $c_1 = 2hc^2$ (mW m^{-2} sr^{-1} (cm^{-1})$^{-4}$) , $c_2 = hc/\kappa$ (K cm), c is the speed of light, κ is the Bolzmann constant, h is the Planck's constant and R_x is the channel integrated "effective" radiance (mW m^{-2} sr^{-1} (cm^{-1})$^{-1}$). The regression coefficients ν_x (cm^{-1}), α_x (-) and β_x (K) are defined by sensor (EUMETSAT, 2012). The estimated absolute error of the linear regression compared to the numerical (spectral integration) solution is in the order of 0.01 K for the BT range 150 – 350 K.

3.5 Simulating the Broad Band VIS Channel

The cloud mask and cloud fractional cover algorithm of GeoSatClim have been developed by assuming the availability of a broad band visible channel on heritage geostationary sensors. The cloud mask and the cloud fractional cover are sensitive to the spectral characteristics of the surface underlying the clouds. While the MSG SEVIRI HRV channel best matches the MFG MVIRI VIS channel it is not available on the full disk. It has to be simulated by use of the linear combination of reflectances of the two narrow-band MSG SEVIRI VIS channels on the full Meteosat disk (Deneke and Roebeling, 2010):

$$\rho_{\mathrm{VIS}} = 0.667\rho_{0.6} + 0.368\rho_{0.8}, \tag{8}$$

where $\rho_{0.6}$ and $\rho_{0.8}$ are the 0.6 μm and 0.8 μm MSG SEVIRI channels. The two narrow band channels do not cover the full spectral bandwidth of the HRV channel. Nevertheless, the above linear approximation explains at least $> 95\%$ of the HRV variance on the full Meteosat disk.

4 Cloud Mask

As outlined in Section 2 and visualized in Figure 2 the SPARC algorithm produces an aggregated rating F from the sum of individual scores A, B, C, D etc.,

$$F = A + B + C + (D) + \ldots \tag{9}$$

where each score generates a continuous measure of cloudiness. It becomes negative for a clear sky and positive for a cloudy scene. The magnitude of the respective score is then a relative measure of cloud occurrence. For instance, a score of 0 often occurs in situations of partial cloudiness or at cloud boundaries. A score of 50 gives a high probability of rather thick clouds. Scores are also allowed to be contradicting. Summing score A of -10 and score B of 10 will yield an aggregated score F=0 and thus result in an undecided cloud mask with low confidence for either cloudy or clear sky. A decision tree misses such functionality. It also cannot cope with missing scores. In SPARC the aggregated rating F can still be calculated when for instance score D (in brackets) is missing.

Substantial changes were made to the original SPARC algorithm for its application to heritage geostationary satellites:

- Use of brightness temperature and reflectance clear sky composites from previous cloud

masked fields instead of fixed background reflectance or NWP-model based skin temperature

- Use of combined spatial and temporal variability instead of just the spatial uniformity texture
- Use of day-night regression instead of a fixed scaling of nighttime to daytime scores
- Substantial reduction of the number of scores due to missing spectral coverage of heritage geostationary sensors such as MVIRI

Similar to hierarchical classification trees cloud masks the aggregated rating of continuous scores method is highly empirical. Each additive score needs to be weighted with at least two coefficients. These coefficients are given in Table 1.

Table 1: Offset and scale factors for each of the cloud mask scores. These factors are valid for the MVIRI and SEVIRI sensor and might need to be adjusted for other sensors.

No.	score	offset	units	scale	units
1	$\mathrm{T_{score}}$	-6.0	K	-0.42	$\mathrm{K^{-1}}$
2	$\mathrm{B_{score}}$	0.05	-	50	-
3	$\mathrm{STR_{score}}$	0	-	100	-
4	$\mathrm{TV_{score}}$	0	K	1	$\mathrm{K^{-1}}$

4.1 Cloud Mask Scores

4.1.1 Temperature Score

The temperature score $\mathrm{T_{score}}$ tests the brightness temperature of the 10.8 μm thermal channel against a background clear sky brightness temperature T_{cf}:

$$\mathrm{T_{score}} = (T_{10.8} - T_{\mathrm{cf}} - \mathrm{T_{offset}})\mathrm{T_{scale}} \tag{10}$$

The key requirement for this score is to estimate a realistic clear sky (cloud free) brightness temperature T_{cf}. Khlopenkov and Trishchenko (2007) use a reanalysis-based skin temperature. This model-based dependency was not found to be a suitable option for regions with complex terrain. In comparison to polar orbiting sensors, geostationary satellite sensors capture the diurnal cycle of brightness temperature which is a good constraint for the T_{cf} retrieval: for each day a diurnal temperature model is fitted on previously cloud masked $T_{10.8}$ data in order to estimate the diurnal cycle of T_{cf} (Section 5.1).

4.1.2 Brightness Score

The brightness-score $\mathrm{B_{score}}$ operates during daytime and it tests the reflectance of the visible channel ρ against a background reflectance ρ_{cf}. The broadband visible channel from MFG MVIRI and the simulated broadband visible channel based on a narrow-to-broadband conversion of the 0.6 and 0.8 μm channels for MSG SEVIRI (see Section 3.5) is used independently from surface type:

$$\mathrm{B_{score}} = (\rho - \rho_{\mathrm{cf}} - \mathrm{B_{offset}})\mathrm{B_{scale}} \tag{11}$$

The key requirement for this score is to estimate a realistic clear sky (cloud free) reflectance ρ_{cf}. Khlopenkov and Trishchenko (2007) use a fixed value of 0.3 (-). This was not found to be a suitable option for the broad range of land and water reflectances found on earth. Similarly, the often used monthly climatological global surface albedo composite datasets like the MODIS albedo (Schaaf et al. (2002); applied for instance as part of the SAFNWC (2013) SEVIRI cloud mask) can yield temporally and spatially non-representative background reflectances with associated cloud mask artifacts. Geostationary satellite sensor data are implicitly the most realistic constraint for ρ_{cf}: contemporary cloud masked ρ data are used in GeoSatClim to invert a diurnal reflectance model of ρ_{cf} (Section 5.2).

4.1.3 Spatio-Temporal Reflectance Variance Score

The spatio-temporal reflectance variance score $\mathrm{STR_{score}}$ compensates for the weakness of the main scores to detect cloud boundaries and low level clouds with a weak reflectance signature. It is calculated by first applying the spatial difference Δ_{xy} (for details see Appendix D) of the broad band visible reflectance for each pixel in a surrounding region of ± 1 pixels. The spatial texture alone is misleading when the background cloud free scene includes a high spatial variance such as in complex terrain and for land-water boundaries. A de-trended temporal standard deviation over ± 1 hours is thus applied to the spatial difference:

$$\mathrm{STR_{score}} = (\sigma'_{\mathrm{t}}(\Delta_{\mathrm{xy}}(\rho)) - \mathrm{STR_{offset}})\mathrm{STR_{scale}}, \tag{12}$$

The $\mathrm{STR_{score}}$ remains low for temporally static but spatially varying surface features and is high for temporally varying and spatially varying atmospheric features. It can be applied during daytime only.

4.1.4 Temporal Temperature Variance Score

The analysis of time variation is possible with geostationary satellite data. The temporal variation of brightness temperature is very effective for the detection of fractional cloud cover. The temporal temperature variance score $\mathrm{TV_{score}}$ is created as follows:

$$\mathrm{TV_{score}} = (\sigma'_{\mathrm{t}}(T_{10.8}) - \mathrm{TV_{offset}})\mathrm{TV_{scale}}, \tag{13}$$

where $\sigma'_{\mathrm{t}}(T_{10.8})$ is the de-trended temporal standard deviation for each pixel centered over ± 1 hours. Details on the calculation of the de-trended temporal standard deviation are given in Appendix D).

4.2 Day-Night Separation

A night factor is calculated to allow a continuous transition of daytime-only to day- and nighttime scores:

$$f_{\mathrm{night}} = (\theta_s^{\mathrm{lim}} - \theta_s)/3, \mathrm{with} 0 \leq f_{\mathrm{night}} \leq 1, \tag{14}$$

and $\theta_s^{\mathrm{lim}} = 85^\circ$ is the maximum daytime solar zenith angle. The night factor becomes 0 at nighttime ($\theta_s > 88^\circ$) and 1 during daytime ($\theta_s < 85^\circ$), with a smooth transition in between.

4.3 Day-Night Regression

The final cloud mask is calculated by adding the individual scores. Less scores are available during nighttime compared to daytime. In order to circumvent a systematic day/night bias in cloud detection, the main nighttime score $\mathrm{T}_{\mathrm{score}}$ is linearly regressed against the two main daytime scores $\mathrm{B}_{\mathrm{score}}$ and $\mathrm{T}_{\mathrm{score}}$ for each day prior to the calculation of the cloud mask:

$$\mathrm{B}_{\mathrm{score}} + \mathrm{T}_{\mathrm{score}} = a_{\mathrm{daynight}} \mathrm{T}_{\mathrm{score}} + b_{\mathrm{daynight}}, \tag{15}$$

where all daily values of $\mathrm{B}_{\mathrm{score}}$ and corresponding values of $\mathrm{T}_{\mathrm{score}}$ with $f_{\mathrm{night}} = 1$ for a given pixel are used in the linear regression (there is one regression per pixel). Khlopenkov and Trishchenko (2007) use fixed values $a_{\mathrm{daynight}} = 2$ and $b_{\mathrm{daynight}} = 0$. Keeping these values dynamic per pixel and day substantially increases the nighttime cloud detection performance. The original values are a fallback solution when the linear regression yields a Pearson correlation coefficient $r < 0.5$ or estimated parameters are unrealistic ($a < 0$ or $a > 10$ or $b < -10$ or $b > 20$). During nighttime $a_{\mathrm{daynight}} \mathrm{T}_{\mathrm{score}} + b_{\mathrm{daynight}}$ is used. During daytime $\mathrm{B}_{\mathrm{score}} + \mathrm{T}_{\mathrm{score}}$ is used.

4.4 Snow Detection

Snow detection is not currently implemented. It is not needed for cloud masking since the “bright” background reflectance of snow covered land surfaces is implicitly removed in all the cloud mask scores through either the subtraction of contemporary clear sky reflectance composites or by only exploiting the spatio-temporal variance instead of the absolute reflectance.

4.5 Cloud Mask Classification

According to the original aggregated rating approach by Khlopenkov and Trishchenko (2007) a cloud mask score $\mathrm{CM}_{\mathrm{score}}$ is calculated by creating a weighted sum of the cloud mask scores:

$$\mathrm{CM}_{\mathrm{score}} = f_{\mathrm{night}}(\mathrm{B}_{\mathrm{score}} + \mathrm{T}_{\mathrm{score}}) + (1 - f_{\mathrm{night}})(a_{\mathrm{daynight}} \mathrm{T}_{\mathrm{score}} + b_{\mathrm{daynight}}). \tag{16}$$

The scores are weighted by a continuous day-night separation flag and employ the day-night re-

gression of the temperature score at night. Compared to Khlopenkov and Trishchenko (2007) and our initial model presented in Stöckli (2013) no spatial or temporal (or combined spatio-temporal) scores are used for the cloud mask score. Comparison with SYNOP data revealed that they do not consistently provide additional skill for cloud detection. It was found here that the spatial or temporal "variance" scores are not statistically independent from the "state" scores and thus cannot be used in a linear additive cloud mask algorithm. The Bayesian CA and CFC calculation in Section 6 demonstrates how these scores are of substantial value if the co-variance structure between scores is properly accounted for.

The two additional weights f_{glint} and f_{snow} introduced in the original algorithm deteriorate the results for the following reason:

1. f_{snow} is not needed here since snow reflectance is explicitly simulated by the clear sky reflectance model. The original model had a fixed background reflectance of 0.3 which is not a suitable choice for highly reflective snow surfaces. In the original model the power of the brightness score thus had to be decreased for snow surfaces.
2. f_{glint} is not needed here since sun glint is explicitly simulated by the clear sky reflectance model. In the original model the power of the brightness score had to be reduced during sun glint since a fixed background value of the ocean reflectance was used.

The $\mathrm{CM}_{\mathrm{score}}$ is only calculated if at least one specific score, the $\mathrm{T}_{\mathrm{score}}$, is present. This constraint allows the spin-up of the cloud mask by use of the clear sky brightness temperature compositing (Section 5) by use of a sensor with only a single thermal channel. This is needed to generate the initial cloud mask for e.g. the MVIRI sensor when no a-priori clear sky reflectance or brightness temperature composite is available or to run the cloud mask with a single (IR) channel. From the continuous cloud mask score a discrete cloud mask classification can be derived:

$$CM = \begin{cases} 0 & \text{if } \mathrm{CM}_{\mathrm{score}} < -4; \\ 1 & \text{if } -4 \leq \mathrm{CM}_{\mathrm{score}} < 4; \\ 2 & \text{if } \mathrm{CM}_{\mathrm{score}} > 4 \end{cases} \tag{17}$$

The thresholds -4 and 4 are chosen such that $CM = 0$ reflects a synoptic cloud amount of ≤ 1 okta (completely cloud free) and $CM = 2$ reflects a synoptic cloud amount ≥ 7 okta (completely cloud covered). $CM = 1$ represents cloud amounts of $2 - 6$ okta

4.6 Cloud Mask Uncertainty

The discretization of the $\mathrm{CM}_{\mathrm{score}}$ to three CM classes masks the continuous nature of the former. During daytime, a $\mathrm{CM}_{\mathrm{score}} \approx 0$ can be the result of a positive $\mathrm{B}_{\mathrm{score}}$ and a negative $\mathrm{T}_{\mathrm{score}}$ and $CM = 1$ has thus to be interpreted as "undecided" cloud mask state. On the other hand, $\mathrm{CM}_{\mathrm{score}} \ll 0$ stands for a highly probable clear sky state while $\mathrm{CM}_{\mathrm{score}} \gg 0$ means a highly probable cloudy state. CM is accompanied by a relative cloud mask uncertainty CM^{σ}. It is large for a $\mathrm{CM}_{\mathrm{score}} \approx 0$ and exponentially decreases towards situations when full cloud cover or full clear sky is observed:

$$\mathrm{CM}^{\sigma} = \exp\left(-\frac{\mathrm{CM}^2_{\mathrm{score}}}{2 \cdot 10^2}\right). \tag{18}$$

CM^{σ} ranges from 0 (low uncertainty) to 1 (high uncertainty). It supplements a clear sky or cloudy state with its uncertainty useful for model inversion (such as the clear sky compositing, see Section 5) or for physical parameter retrieval (e.g. cloud optical thickness or surface albedo). It has to be noted that CM^{σ} is not an absolute quantity. It is best used to weight the quality of subsequent clear sky or cloudy observations relative to each other. CM^{σ} is high at cloud boundaries and during night when only a single channel is used. In order to generate an absolute uncertainty measure the bayesian cloud fraction approach has to be used (Section 6).

4.7 Cloud Top Height

Cloud top height CTH (m) is calculated by assuming a constant atmospheric lapse rate $\lambda_{\mathrm{a}} = 0.0065$ K m^{-1}. With a single infrared channel the CTH is only strictly valid for opaque clouds:

$$\mathrm{CTH} = \frac{T_{10.8} - T_{\mathrm{cf}}}{\lambda_{\mathrm{a}}} \tag{19}$$

where $T_{10.8}$ is the all sky brightness temperature of the 10.8 μm channel and T_{cf} is the clear sky brightness temperature from the clear sky compositing of Section 5. The formula assumes that the ToA clear sky brightness temperature T_{cf} is a surrogate for the 2 m air temperature. For semi-transparent clouds the brightness temperature contains a mixture of surface and cloud information which leads to an underestimation of the cloud top height. Stephens (1994) suggest a correction by use of the different thermal emissivities of the earth's surface compared to ice clouds which continuously decreases for semi-transparent and fully vanishes opaque clouds. Such a correction is not applicable with a single broad-band infrared channel. The CTH implementation in GeoSatClim is based on the requirement to separate low-level opaque clouds from middle- and high-level clouds for the downstream FTH retrieval (RD-2).

Cloud height is given relative to the orographic height (the mean orographic height of the 10.8 μm channel resolution). Cloud height is set to missing for clear sky pixels ($CM = 0$, see the cloud mask in Section 4).

4.8 Cloud Top Pressure

Cloud top pressure CTP (hPa) is calculated with the international barometric height formula constrained by a linear temperature gradient in the troposphere based on the U.S. standard atmosphere 1976 (AFGL-TR-86-0110):

$$\mathrm{CTP} = p_0 \left(1 + \lambda_{\mathrm{a}} \frac{\mathrm{CTH} + \mathrm{Z}}{T(h_0)}\right)^{5.255}, \tag{20}$$

with $h_0 = 0$ m, $p_0 = 1013.25$ hPa, $T(h_0) = 288.15$ K and Z (m) is the mean orographic height of the satellite pixel.

5 Clear Sky Compositing

Clear sky compositing for visible reflectances and infrared brightness temperatures is performed once per day at 00:00 UTC. Clear sky compositing has the following goals:

- reconstruct a full diurnal cycle of clear sky ToA states from irregular (gaps due to cloud cover) cloud masked ToA states,
- remove cloud or cloud shadow driven noise in cloud masked ToA states,
- provide a current set background states for the next cloud mask calculation.

The clear sky compositing of reflectance and brightness temperature employs parametrized models that are inverted on a pixel-by-pixel basis to the daily course cloud free states from previous days and previous iterations on the same day. Cloud free states are weighted by use of both the pixel's age CM^t (days) and its cloud mask uncertainty CM^σ (-) for each cloud free state:

$$w = \left[\mathrm{CM}^\sigma + \max(\mathrm{CM}^t, 0.5)/\mathrm{CM}^t_{\max}\right]^{-1}, \tag{21}$$

where $\mathrm{CM}^t_{\max} = 7$ (days) is the maximum allowed age for a clear sky state. Older states are discarded. Thus, the more recent a clear sky state or the higher its probability of being fully clear sky, the higher the weight it receives during the diurnal reflectance and brightness temperature fitting process.

5.1 Clear Sky Brightness Temperature

The clear sky brightness temperature T_{cf} is needed by the cloud mask (Section 4) in order to calculate the temperature score. T_{cf} can only be derived after the $T_{10.8}$ channel data have been separated into clear sky and cloudy data. This chicken and egg causality is often found in cloud masks that generate their own boundary conditions in order to be less dependent on external (often model-based) data sets. The problem is solved here by initializing the system with external constraints and then letting it become self-consistent after spin-up. 6-hourly surface skin temperature forecasts are ingested from the ECMWF ERA Interim (Berrisford et al., 2009; Dee et al., 2011) and are used in the initial fitting process for the diurnal course of the clear sky brightness temperature T^0_{cf}. Surface skin temperature SKT (K) [2] is corrected for subgrid-scale topography and for the total column water vapor in the satellite's view path:

$$T^0_{\mathrm{cf}} = \mathrm{SKT} + (Z - Z_{\mathrm{ecmwf}})\lambda_{\mathrm{a}} - \frac{\mathrm{TCWV}\exp\frac{Z_{\mathrm{ecmwf}} - Z}{H_{\mathrm{a}}}}{5 \cdot \max(\cos(\theta_{\mathrm{v}}), 0.5)}, \tag{22}$$

[2] Surface skin temperature is the NWP analogue of the radiative land surface temperature from satellite retrievals

where a constant atmospheric lapse rate $\lambda_{\mathrm{a}} = 0.0065$ K m^{-1} for the vertical temperature gradient and a constant atmospheric scale height of $H_{\mathrm{a}} = 1000$ m for the vertical TCWV distribution is used. TCWV is the total column water vapor (kg m^{-2}). Z and Z_{ecmwf} (m) are the orographic altitude of the satellite pixel and the ECMWF grid cell. θ_{v} is the satellite view zenith angle. This is a highly empirical inverse atmospheric correction of surface skin temperature and is applicable since SKT is used during spin up only. In a later stage an inversion of the LST retrieval algorithm (RD-1) should be implemented. Since uncertainty is not part of the ECMWF data, a weight of 2.0 is assigned to ECMWF skin temperature data. This weight is derived by use of $\mathrm{CM}^t = 0$ days and $\mathrm{CM}^\sigma = 0$ for the weights calculation in Section 5. After cloud screened $T_{10.8}$ become available from cloud screening after spin-up, they replace the ECMWF skin temperature data. ECMWF skin temperature data continues to be ingested during processing. They are used as a backup when long term cloud cover ($> \mathrm{CM}^t_{\mathrm{max}}$) inhibits the compositing of clear sky brightness temperature or consecutive gaps of more than 6 hours exist in the cloud masked clear sky brightness temperature data. This gap test is required to ensure that the model inversion is based on diurnally evenly distributed data.

The diurnal cycle of clear sky brightness temperature T_{cf} is calculated by fitting a curve through all valid clear sky retrievals of $T_{10.8}$ (respectively, four ECMWF derived T^0_{cf} values at 0, 6, 12 and 18 UTC for the first fit). Outliers in $T_{10.8}$ are removed by only considering the 5-100% percentile for the clear sky diurnal time series of each pixel (except for very strong surface layer inversions only low outliers can occur, due to missed clouds during cloud screening).

For the diurnal temperature modeling the following sun orbital parameters need to be calculated. True solar time t (hours) is calculated from UTC (hours):

$$t = \mathrm{UTC} + \lambda/15, \tag{23}$$

where λ is the longitude (degrees east) and t is cyclic within the bounds $0 \ldots 24$. The sun's declination δ (degrees) is approximated by:

$$\delta = 23.45 \sin\left(\frac{2\pi}{365}(D + 284)\right), \tag{24}$$

where D is the Day of Year ($1 \ldots 365$; leap years are constrained to 365 days for simplicity).

The diurnal cycle of clear sky T_{cf} is modeled by fitting either the thermal model by Mannstein et al. (1999) using 3 free parameters or by Göttsche and Olesen (2009) using 6 free parameters to the diurnal distribution of observed clear sky $T_{10.8}$ values. The Mannstein et al. (1999) model is chosen in the case when less than 7 clear sky observations are present for the whole day. ECMWF skin temperature values are ingested when less than 4 clear sky observations are available, such as for instance during prolonged periods of constant cloudiness. Both models are suitable to represent the diurnal cycle of clear sky radiative surface temperature, which is needed as reference for cloud screening. The model by Göttsche and Olesen (2009) however includes a more realistic representation of the insolation which drives the clear sky surface temperature and it better captures the inter-day trends.

5.1.1 Mannstein Model

The diurnal surface temperature model by Mannstein et al. (1999) is a highly empirical and simplified solution to the daytime solar heating process of the earth's surface. The three parameter model simulates the typical bell-shaped curve of the clear sky land surface radiative temperature and was modified by Dürr et al. (2013) to include both a sine and an exponential term. The number of daylight hours N_d (hours) is first calculated:

$$N_d = \frac{24}{\pi} \arccos(\min(\max(-\tan\phi \cdot \tan\delta, -1), 1)), \tag{25}$$

where ϕ is the latitude (degrees [3] N) and $N_d > 0.01$. The diurnal course of clear sky brightness temperature is then calculated:

$$T_{\mathrm{cf}}(t) = T_{\min} + T_{\mathrm{a}} \left[\exp\left(\max\left(-8 \left(\frac{t - t_{\mathrm{m}}}{N_d} \right)^2, -50 \right) \right) + 0.1 \sin\left(\frac{\pi}{12}(t - t_{\mathrm{m}}) \right) \right]. \tag{26}$$

The exponential function [4] describes daytime heating of the surface by use of a Gaussian curve and the sinusoidal term accounts for a time-lagged decay of radiative surface temperature after sunset. The function is analytical, has cyclic boundary conditions and can be differentiated. It contains three free parameters: minimum daily temperature $T_{\min}$ (K), diurnal temperature amplitude T_{a} (K) and t_{m} (hours), the solar time of maximum heating. These three parameters can be estimated by use of a robust non-linear least square solver (http://www.physics.wisc.edu/~craigm/idl/fitting.html) based on MINPACK-1 (http://www.netlib.org/minpack). Start values and parameter bounds are found in Table 2.

Table 2: Parameters of the Mannstein et al. (1999) model

No.	name	start value	lower bound	upper bound
1	$T_{\min}$	$\min(T_{10.8})$	$\min(T_{10.8}) - 5$	$\min(T_{10.8}) + 5$
2	T_{a}	$\max(T_{10.8}) - \min(T_{10.8})$	0	$\max(T_{10.8}) - \min(T_{10.8}) + 5$
3	t_{m}	12.5	12	15

Table 3: Geographic locations of the sites used for the clear sky brightness temperature and reflectance model examples. Elevation is given as elevation above sea level and is the mean Meteosat pixel altitude (and not the exact site altitude).

No.	name	longitude (° E)	latitude (° N)	elevation (m)	θ_{v} (°)	land use type
1	Payerne	6.942322	46.812242	505	54.6	temperate grassland
2	Toravere	26.462	58.254	64	70.9	boreal grassland
3	Eggishorn	8.092742	46.426560	1584	54.4	boreal barren / rock
4	Glint	40.0111	17.07452	0	53.9	deep ocean

Figure 5 upper left panel demonstrates that the three parameter model is robust to data quality issues: at noon the clear sky composite become affected by partially cloudy clear sky brightness temperature observations. This cloud-related temperature signature of 1-3 K is not detected with

[3] Note that all angles in this document are given in units degrees. They have to be converted to units radians when they are used as arguments to trigonometric functions except when otherwise noted

[4] The exponent is limited to > -50 to circumvent numeric underflow

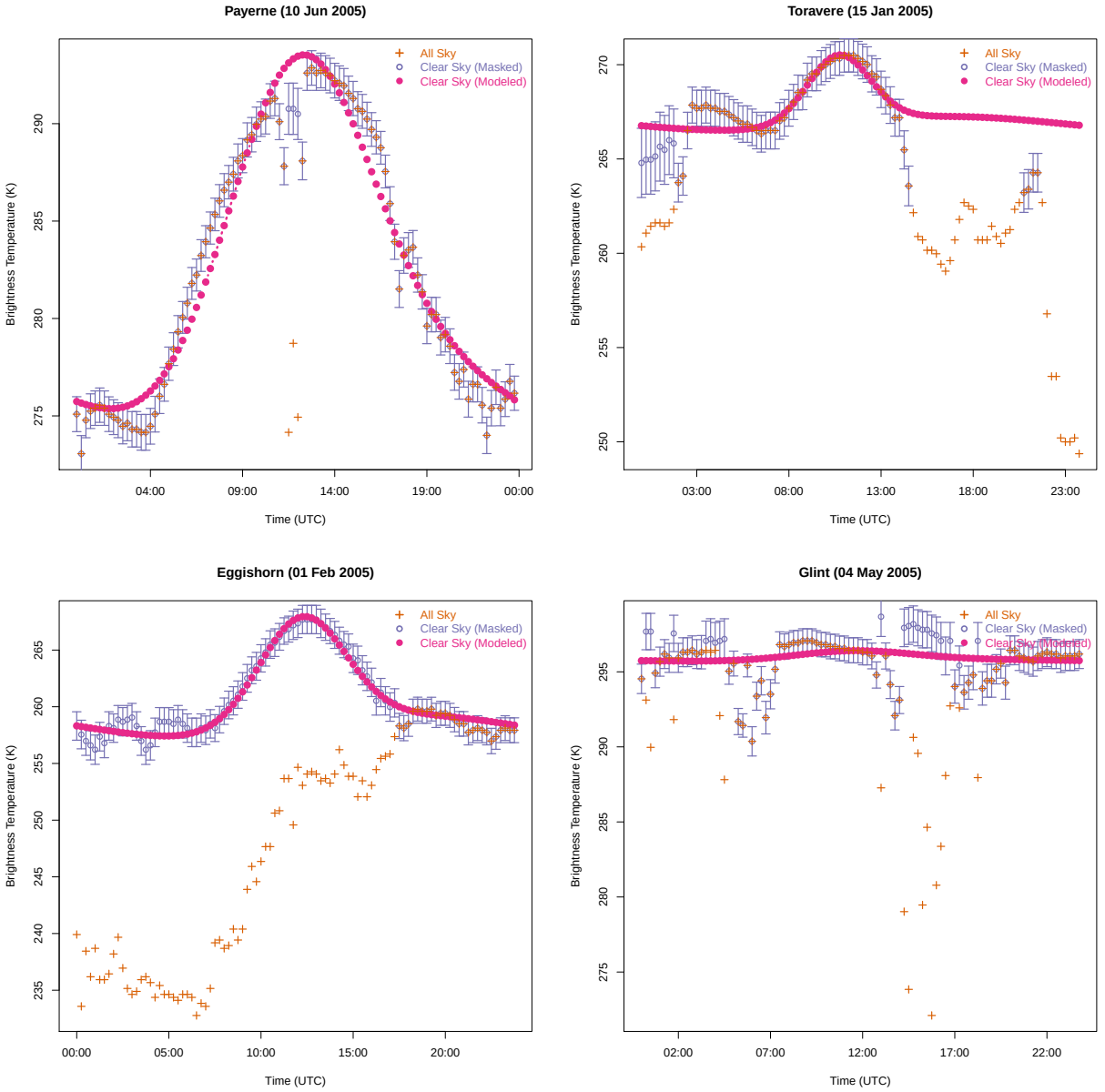

Figure 5: Examples of the diurnal temperature model after Mannstein et al. (1999) at four sites given in Table 3. Meteosat all sky (orange crosses), cloud masked (blue circles including cloud mask uncertainty) and corresponding modeled clear sky (pink filled circles) ToA brightness temperature.

the 2 channel cloud mask. The three larger outliers during noon have a temperature signature of 10-15 K and are masked. The model effectively mitigates the effect of individual cloud-affected observations. Increasing robustness is one of the main benefits of using a parametric model of the diurnal cycle instead of doing classical “slot-by-slot” temporal compositing.

However, for Payerne the Mannstein et al. (1999) model cannot fully represent the continuous transition between the end of the night and the rapid increase of the T_{cf} after sunrise. It also is not able to fully account for the complex surface heating during daytime: the width of the bell-shape curve is underestimated. The model further has cyclic boundary conditions, which might be violated when synoptic weather conditions yield substantial temperature changes from one day to the next.

The Mannstein et al. (1999) model uses only three parameters and is ideally suited to fit a "rough" diurnal course of T_{cf} with few cloud free observations available. This is demonstrated in the upper right panel of Figure 5: at Toravere during wintertime using a view zenith angle $> 70°$ only a partial day worth of cloud free observations are available. And the remaining observations have a higher uncertainty (larger blue error bars) compared to Payerne. The model can simulate clear sky brightness temperature for parts of the day where no observations are available. The model is also able to simulate diurnal cycles with a weak amplitude such as shown in the lower left panel for the snow covered Alpine site Eggishorn. And it can be used to represent clear sky brightness temperature for ocean areas with no diurnal cycle at all.

5.1.2 Göttsche Model

The model is modified after Göttsche and Olesen (2009) to simulate a non-cyclic but continuous course of the clear sky diurnal temperature evolution including the night-time decay of the previous day prior to sunrise. All equations are given here for completeness but the original reference may be consulted for an in-depth explanation of the algorithm itself. The diurnal course of clear sky brightness temperature is calculated for three different parts of the diurnal cycle separated by the "thermal" hour angle θ_{h} (radians): sunrise θ_{r} and sunset θ_{s}:

$$T_{\mathrm{cf}}(\theta) = T_{\min} + \frac{t}{24}\delta T + \begin{cases} \left[T_{\mathrm{a}} \cos\theta_{\mathrm{zs}} \dfrac{e^{\tau(m_{\min} - m(\theta_{\mathrm{zs}}))}}{\cos(\theta_{\mathrm{z,\,min}})}\right] \dfrac{w_t k}{k + \frac{12(\theta_{\mathrm{h}} - \theta_{\mathrm{s}} + \Delta t_{D-1})}{\pi}} & \text{if } \theta_{\mathrm{h}} < \theta_{\mathrm{r}} \\ T_{\mathrm{a}} \cos(\theta_{\mathrm{z}}) \dfrac{e^{\tau(m_{\min} - m(\theta_{\mathrm{z}}))}}{\cos\theta_{\mathrm{z,\,min}}} & \text{if } \theta_{\mathrm{r}} \le \theta_{\mathrm{h}} < \theta_{\mathrm{s}} \\ \left[T_{\mathrm{a}} \cos\theta_{\mathrm{zs}} \dfrac{e^{\tau(m_{\min} - m(\theta_{\mathrm{zs}}))}}{\cos(\theta_{\mathrm{z,\,min}})}\right] \dfrac{w_t k}{k + \frac{12(\theta_{\mathrm{h}} - \theta_{\mathrm{s}})}{\pi}} & \text{if } \theta_{\mathrm{h}} \ge \theta_{\mathrm{s}}, \end{cases} \quad (27)$$

where θ_{h} (radians) is the "thermal" hour angle:

$$\theta_{\mathrm{h}} = (1 - w_\theta)\frac{\pi}{12}(t - 12) + w_\theta \frac{\pi}{12}(t - t_{\mathrm{m}}) \quad (28)$$

It corresponds exactly to the solar hour angle at sunrise but is continuously shifted to the "thermal" noon at local solar time t_{m} due to the thermal inertia of both the surface and the near-surface atmosphere. The weight w_θ is 0 at sunrise and 1 at t_{m}. $\theta_{\mathrm{r}} = arccos((-\sin\delta \sin\phi/(\cos\delta\cos\phi))$ (radians) is the hour angle of sunrise (θ_{r} is set to $-\theta_{\mathrm{r}}$ if positive) and $\theta_{\mathrm{s}} = \frac{\pi}{12}(t_{\mathrm{s}} - t_{\mathrm{m}})$ (radians) is the thermal hour angle when "thermal" sunset occurs, with respect to the "thermal" noon at local solar time t_{m}. $\theta_{\mathrm{z}} = \arccos(\sin\delta\sin\phi + \cos\delta\cos\phi\cos\theta_{\mathrm{h}})$ (radians) is the sun zenith angle for hour angle θ_{h} (analogous formulation for θ_{zs} at zenith angle θ_{s} and for the minimum zenith angle $\theta_{\mathrm{z,\,min}}$ at "thermal" noon $\theta_{\mathrm{h}} = 0$). Compared to the original reference the decay after sunset and before sunrise is calculated by a hyperbolic instead of an exponential function and the day-to-day temperature rise δT is linear over the whole 24 h instead of just after sunset. This choice is based on own tests showing a higher performance of the hyperbolic formulation and findings of Duan et al. (2012, 2013). Prior to sunrise the previous day's temperature decay is calculated by using the decay constant k of the present day. $\Delta t_{D-1} = 2\pi - (t_{\mathrm{m}} - 12)\pi/12$ is the diurnal time shift required for applying the present day's after-sunset decay function to the time steps prior to sunrise. The weight w_t is required to force the hyperbolic decay exactly to $T_{\min} + \delta T$ for the present day's decay and to $T_{\min}$ for the previous day's decay.

$$w_t = \begin{cases} \frac{\theta_\mathrm{h}-\theta_\mathrm{s}+\Delta t_{D-1}}{\theta_\mathrm{r}-\theta_\mathrm{s}+\Delta t_{D-1}} & \text{if } \theta_\mathrm{h} < \theta_\mathrm{r} \\ \frac{\theta_\mathrm{h}-\theta_\mathrm{s}}{\theta_\mathrm{r}-\theta_\mathrm{s}+\Delta t_{D-1}} & \text{if } \theta_\mathrm{h} \geq \theta_\mathrm{s}. \end{cases} \tag{29}$$

This model includes an explicit but simplified simulation of the clear sky atmospheric transmission, which has a significant impact on the surface energy budget. The optical air mass m (-) is calculated in dependence of the sun zenith angle θ_z after Vollmer and Gedzelmann (2006):

$$m(\theta_\mathrm{z}) = -\frac{R_E}{H}\cos\theta_\mathrm{z} + \sqrt{\left(\frac{R_E}{H}\cos\theta_\mathrm{z}\right)^2 + 2\frac{R_E}{H} + 1}, \tag{30}$$

where $R_E = 6371000$ m is the earth's radius and $H = 8430$ m is the scale height of the dry atmosphere. The exponential decay constant k can be calculated by assuming differentiability everywhere and setting the derivatives of both equations for $T_\mathrm{cf}(\theta)$ equal at θ_s:

$$k = \frac{12}{\pi\frac{\partial\theta_\mathrm{z}(\theta_\mathrm{s})}{\partial\theta_\mathrm{s}}}\frac{\cos\theta_\mathrm{zs}}{\sin\theta_\mathrm{zs} + \tau\cos\theta_\mathrm{zs}\frac{\partial m(\theta_\mathrm{zs})}{\partial\theta_\mathrm{zs}}}, \tag{31}$$

and where

$$\frac{\partial\theta_\mathrm{z}(\theta_\mathrm{s})}{\partial\theta_\mathrm{s}} = \frac{\sin\theta_\mathrm{s}\cos\delta\cos\phi}{\sin\delta\sin\phi + \cos\delta\cos\phi\sin\theta_\mathrm{s}}, \tag{32}$$

and where

$$\frac{\partial m(\theta_\mathrm{zs})}{\partial\theta_\mathrm{zs}} = \frac{R_E}{H}\cos\theta_\mathrm{zs} - \frac{\frac{R_E^2}{H^2}\cos\theta_\mathrm{zs}\sin\theta_\mathrm{zs}}{\sqrt{\left(\frac{R_E}{H}\cos\theta_\mathrm{zs}\right)^2 + 2\frac{R_E}{H} + 1}}. \tag{33}$$

The model contains six free parameters: the minimum daily temperature T_min (K), diurnal temperature amplitude T_a (K), the solar time of maximum heating t_m (hours), the solar time of "thermal" sunset t_s (hours), the temperature difference between two consecutive days δT (K) and the atmospheric optical thickness τ (-). Compared to the original formulation not τ but e^τ is chosen since it allows a more efficient parameter estimation (the result is more linearly related to e^τ than to τ). These six parameters can be estimated by use of a robust non-linear least square solver (http://www.physics.wisc.edu/~craigm/idl/fitting.html) based on MINPACK-1 (http://www.netlib.org/minpack). Start values and parameter bounds are found in Table 4. The numerical fixes required in the model are: $t_\mathrm{s} > t_\mathrm{m}$ and $k > 1$.

Table 4: Parameters of the Göttsche and Olesen (2009) model

No.	name	start value	lower bound	upper bound
1	T_min	$\min(T_{10.8})$	$\min(T_{10.8}) - 5$	$\min(T_{10.8}) + 5$
2	T_a	$\max(T_{10.8}) - \min(T_{10.8})$	0	$\max(T_{10.8}) - \min(T_{10.8}) + 5$
3	t_m	12.5	12	15
4	t_s	17	14	20
5	δT	0	-5	5
6	e^τ	1.5	1	3

The Göttsche and Olesen (2009) model does not have cyclic boundary conditions and it includes a more realistic representation of the pre-dawn temperature decay and the solar heating of the earth's

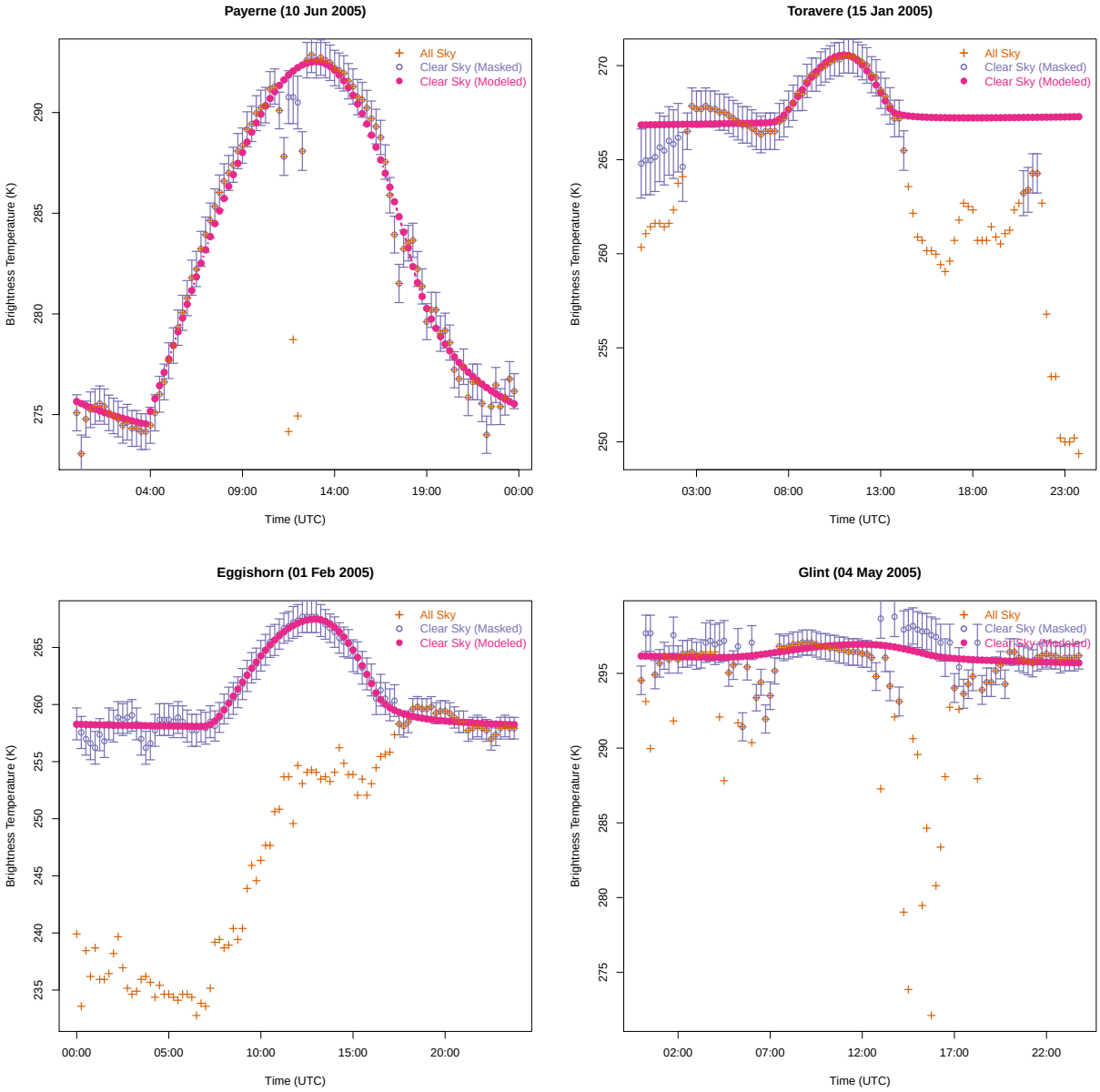

Figure 6: Examples of the diurnal temperature model after Göttsche and Olesen (2009) at four sites given in Table 3. Meteosat all sky (orange crosses), cloud masked (blue circles including cloud mask uncertainty) and corresponding modeled clear sky (pink filled circles) ToA brightness temperature.

surface. Figure 6 demonstrates that it is able to accommodate changes in day-to-day surface temperature conditions and the continuous response of T_{cf} at sunrise is realistically simulated. The model specifically reproduces the asymmetric shape of the diurnal course of T_{cf} between morning and afternoon hours, which results in much more realistic slopes of the rising T_{cf} during morning hours compared to Figure 5. Like the Mannstein et al. (1999) model it is able to reconstruct the diurnal course of T_{cf} even when a substantial part of the day is missing clear sky brightness temperature observations.

The Göttsche and Olesen (2009) model uses six parameters and provides a realistic empirical approximation of the diurnal course of T_{cf} for a wide range of surfaces types and surface states. The

fitting of six instead of three parameters, combined with a more complicated formulation, however make it around 5–10 times more computationally demanding when compared with the Mannstein et al. (1999) model.

5.2 Clear Sky Reflectance

The clear sky reflectance ρ_{cf} is needed as a reference by the cloud mask to calculate the brightness score (Section 4). Many cloud mask algorithms choose either a fixed background value e.g. depending on land use type or make use of externally derived mean monthly "albedo" climatologies (e.g. the MODIS albedo dataset). These methods may introduce temporal and spatial inconsistencies in cloud masking since the clear sky surface reflectance can have a substantial diurnal cycle due to surface anisotropy and clear sky atmospheric turbidity and spatial variability is substantially large, e.g. at land/sea boundaries or in mountainous regions. A monthly composite can also be problematic during times of rapid changes in surface reflectance (green-up, snow fall, snow melt). Geostationary satellite data contains all this valuable information on the continuous diurnal course of clear sky reflectance, which is often discarded.

In "GeoSatClim " the diurnal course of the clear sky reflectance ρ_{cf} is calculated by fitting a parameterized curve through all valid and most recent clear sky retrievals covering the whole diurnal cycle. Such a statistical method connects the large number of diurnal clear sky measurements and maximizes the usage of information available from geostationary sensors. In turn, the maximum required compositing period decreases to a few ($\mathrm{CM}^{t}_{\mathrm{max}}$) days. The model is built on the Modified Lambert-Beer equations (Müller et al., 2004) for atmospheric scattering, the back-scattering properties of land surfaces (Zelenka et al., 1999) and the terrain-dependent illumination conditions (Tan et al., 2010):

$$\rho_{\mathrm{cf}} = \rho_0 \cdot A \cdot B \cdot G \cdot I, \tag{34}$$

where A is the contribution of atmospheric absorption and scattering; B is the contribution of surface reflectance backscatter and the hotspot effect over land; G is the sun glint (specular reflection) over water; and I is the contribution of illumination in terrain. ρ_0 is the diurnally invariant clear sky ToA base reflectance. The atmospheric component is modeled after Rahman et al. (1993), the land hotspot after Zelenka et al. (1999), the sun glint after Berendes et al. (1999) and Dybbroe et al. (2005) and the illumination correction after Meyer et al. (1993):

$$A = \frac{(\cos\theta_{\mathrm{s}})^{a-1} \cdot (\cos\theta_{\mathrm{v}})^{a-1}}{(\cos\theta_{\mathrm{s}} + \cos\theta_{\mathrm{v}})^{1-a}} \tag{35}$$

$$B = 1 + b\left(\frac{\max\left(\delta_{\mathrm{b}}^{\max} - \delta_{\mathrm{b}}, 0\right)}{\max\left(\delta_{\mathrm{b}}^{\max} - \delta_{\mathrm{b}}^{\min}, 1\right)}\right)^2 \tag{36}$$

$$G = 1 + g \cdot e^{-0.5\left(\frac{\delta_{\mathrm{f}}}{\delta_{\mathrm{f}}^{\max}}\right)^2} \tag{37}$$

$$I = \frac{\cos\theta_{\mathrm{s-t}} + c}{\cos\theta_{\mathrm{s}} + c} \tag{38}$$

where θ_s is the sun zenith angle, θ_v is the view zenith angle and a is an empirical parameter specifying the atmospheric transmissivity. δ_b and δ_f are the sun-satellite backward and forward scattering angles (Appendix C), δ_b^{min} is the minimum sun-satellite backward scattering angle during the day (e.g. at solar noon, when $\phi_{v-s} = 0$). The backscatter (hotspot) effect is largest when the sun is exactly behind the satellite sensor (low backward scattering angle). δ_b^{max} is the maximum sun-satellite backward scattering angle giving the width of the hotspot curve and b specifies the magnitude of the hotspot. The sun glint effect is largest when the forward scattering angle is low. δ_f^{max} gives the maximum forward scattering angle for the sun glint function.

The illumination function was originally developed to correct Landsat reflectances in topographically complex terrain. It also applies to Meteosat data and it corrects for diurnal differences in both atmospheric load and land anisotropy. θ_{s-t} is the angle between the sun direction and normal to the terrain (Appendix C) and c is an empirical parameter specifying the magnitude of diffuse to global irradiance. Due to uncertainty in geo-registration of heritage satellite data, pixel-wise terrain parameters estimated from topographic models can be unrealistic (e.g. a south-facing slope can easily be shifted to a north facing pixel with a 1 km geo-registration error). Due to this limitation it was chosen to have the pixel-wise terrain slope θ_t (degrees) and terrain aspect ϕ_t (degrees, clockwise from north) as free parameters, so the illumination function transforms to:

$$I = \frac{\cos\theta_t \cos\theta_s + \sin\theta_t \sin\theta_s \cos(\phi_t - \phi_s) + c}{\cos\theta_s + c}, \tag{39}$$

For land $G = 1$ and for water $B = 1$.The model parameters ρ_0, a, b (land), δ_b^{max} (land), g (water), δ_f^{max} (water), c, θ_t and ϕ_t are estimated by use of a robust non-linear least square solver (http://www.physics.wisc.edu/~craigm/idl/fitting.html) based on MINPACK-1 (http://www.netlib.org/minpack). Start values and parameter bounds are found in Table 5. Fitting is performed only if the longest gap in the observed clear sky data over the diurnal cycle is no longer than 7 hours and if at least 8 (number of free parameters plus 1) clear sky reflectances are available from previous cloud maskings which are not older than CM_{max}^t days. Illumination parameters are also estimated for water in order to account for partial land/water pixels and to correctly fit atmosphere or surface anisotropy driven diurnal reflectance changes. Fitted reflectances with $\rho < 0.01$ or $\rho > 1.25$ are discarded.

A simpler model without illumination correction using only the terms A, B and G with three parameters ρ_0, a and b is chosen for prolonged cloudy periods when less than 8 clear sky observations are available from the previous days. With 4-7 input reflectances, the above functions modify to: $I = 1$, $\delta_b^{max} = 70$ and $\delta_f^{max} = 10$.

Figure 7 demonstrates that the “simple” 3 parameter diurnal reflectance model has substantial skill to reproduce the clear sky reflectance of two out of the four exemplified locations (For details see Table 3). Except for the underestimated width of the BRDF backscatter during mid-day the diurnal course at Payerne is well simulated. The perfect match for the diurnal asymmetry at Toravere is a result of the combined high view zenith and changing sun zenith in the A “atmospheric” term of the model. The two lower panels however show the limitation of this model: the Eggishorn pixel is located on a south-western slope and it is affected by shading during the morning and the terrain-sun geometry yield a higher reflectance during the afternoon. This asymmetry cannot be represented by the 3 parameter model. A similar problem exists in areas with sun glint: the diurnally asymmetric reflectance due to sun-glint in the morning is not simulated by the 3 parameter model.

Table 5: Parameters of the clear sky reflectance model

No.	name	start value	lower bound	upper bound
		Land		
1	ρ_0	0.1	0.01	1
2	a	0.75	0	5
3	b	0.4	0	5
4	$\delta_{\mathrm{b}}^{\max}$	70	50	120
5	c	0.5	0.1	5
6	θ_{t}	5	0	35
7	ϕ_{t}	180	10	350
		Water		
1	ρ_0	0.05	0.01	1
2	a	0.75	0	5
3	g	0.4	0	5
4	$\delta_{\mathrm{f}}^{\max}$	10	5	50
5	c	0.5	0.1	5
6	θ_{t}	5	0	35
7	ϕ_{t}	180	10	350

Figure 8 demonstrates that the “advanced” 7 parameter diurnal reflectance model has substantial skill to reproduce the clear sky reflectance of all four exemplified locations (For details see Table 3). It includes the estimation of the width of the land backscatter (hotspot) effect (Payerne) and is able to estimate the illumination contribution of sloped terrain and sun glint effects as shown in the lower panel. The fitting of seven parameters combined with a more complicated formulation is the default clear sky reflectance model in GeoSatClim when 8 or more input clear sky reflectances are available. It is however around 5–10 times more computationally demanding compared to the three parameter clear sky reflectance model which is used when 4–7 clear sky input reflectances are available.

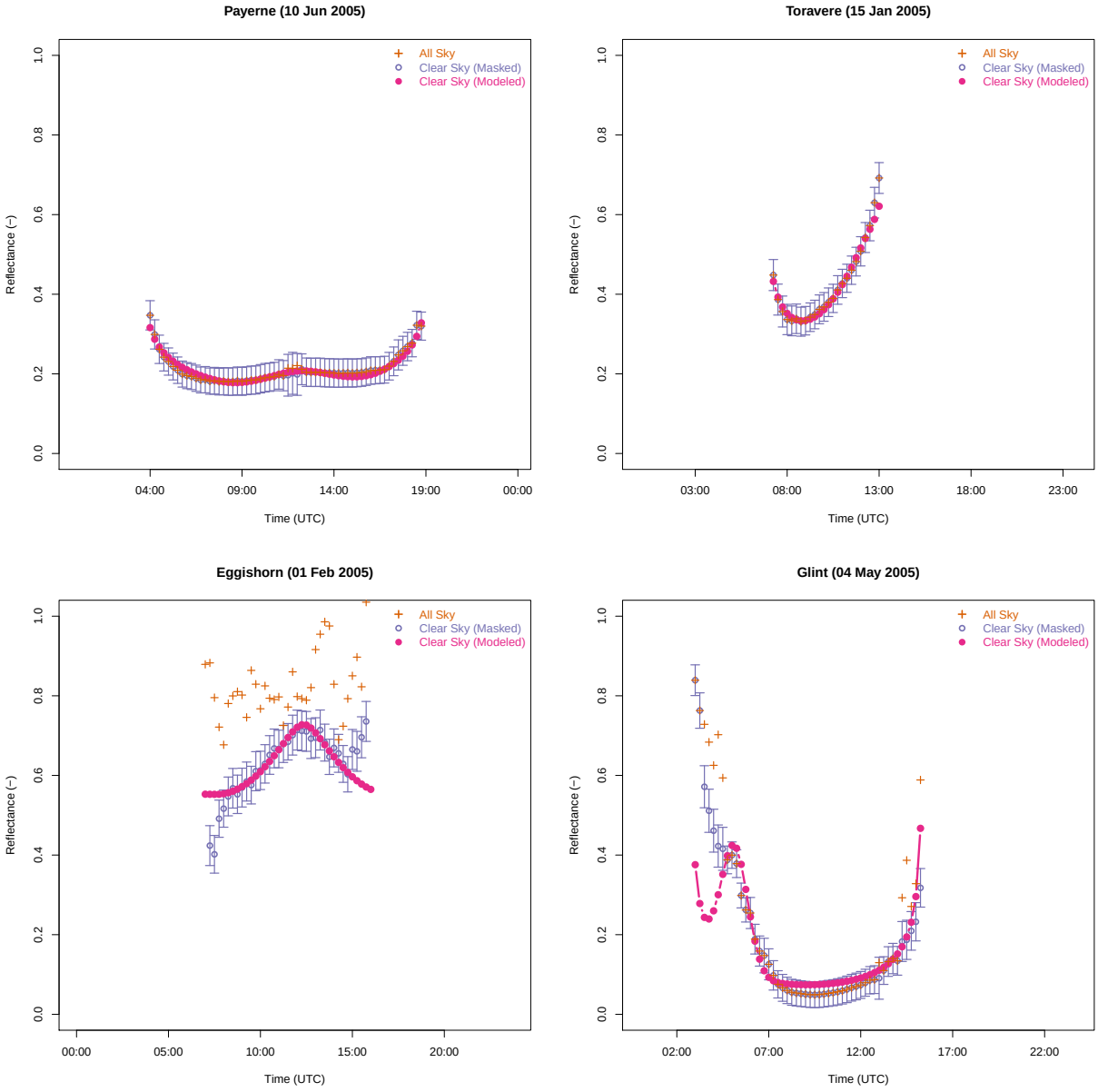

Figure 7: Examples of the diurnal clear sky reflectance model using only 3 parameters at four sites given in Table 3. Meteosat all sky (orange crosses), cloud masked (blue circles including cloud mask uncertainty) and corresponding modeled clear sky (pink filled circles) ToA reflectance.

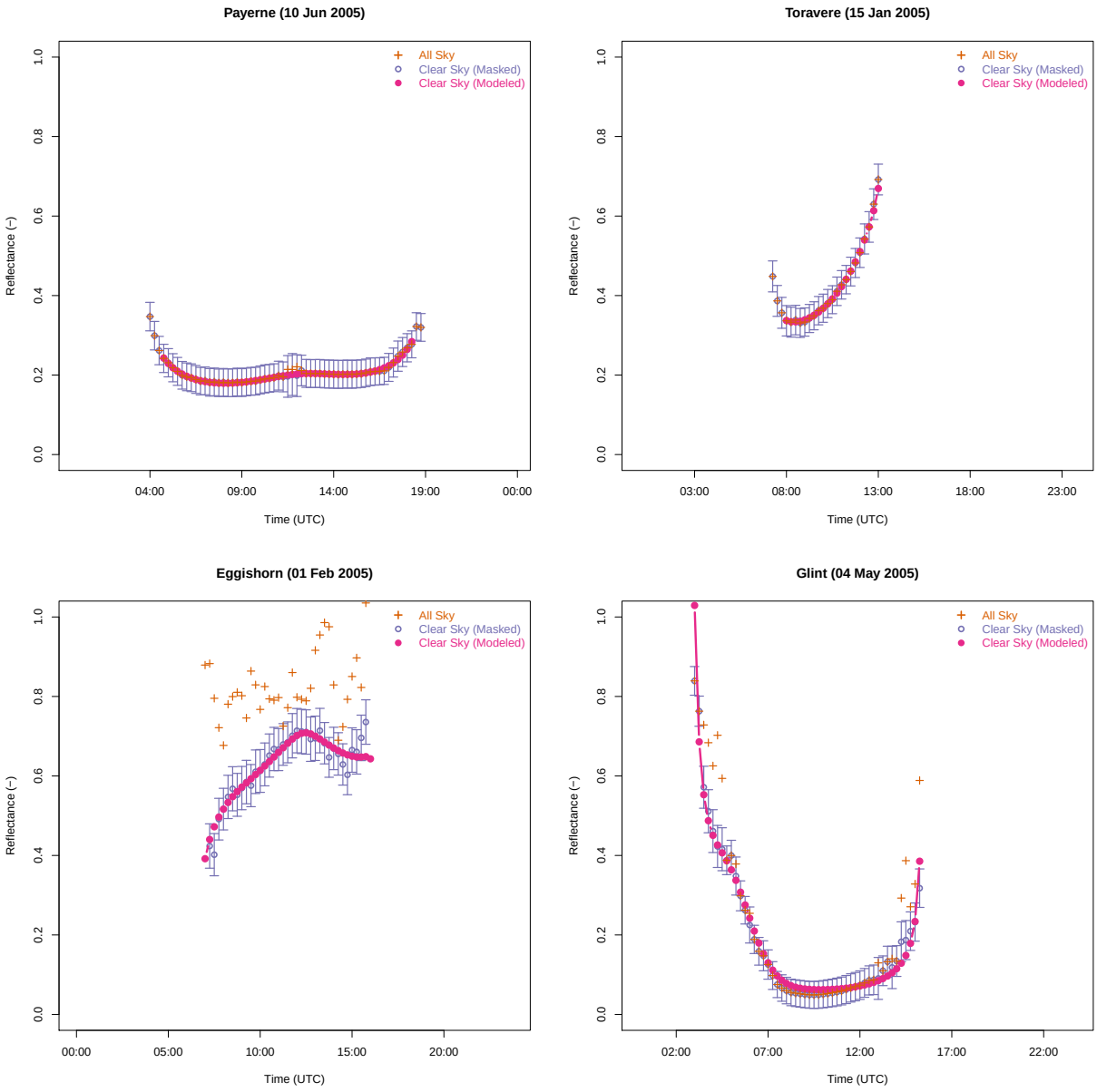

Figure 8: Examples of the diurnal clear sky reflectance model using all 7 parameters at four sites given in Table 3. Meteosat all sky (orange crosses), cloud masked (blue circles including cloud mask uncertainty) and corresponding modeled clear sky (pink filled circles) ToA reflectance.

6 Cloud Fraction

Cloud Fractional Cover (CFC) and Cloud Amount (CA) are estimated for each Meteosat pixel with a Bayesian classifier which employs a subset of the continuos cloud mask scores and clear sky states described in Sections 4.1 and 5.

6.1 Bayes Theorem in Cloud Detection

The Bayes theorem has been successfully applied to the cloud masking problem (Heidinger et al., 2012; Hollstein et al., 2014; Karlsson et al., 2015). The implementation of the Bayes theorem is numerically simple and it involves few arithmetic calculations. It however requires a homogeneous observational constraint which best covers the full range of the cloud mask spatial and temporal domain. The general application of the Bayes theorem to the cloud masking problem can be summarized as follows:

$$P(C|F) = \frac{P(C)P(F|C)}{P(F)}, \tag{40}$$

where $P(C|F)$ is the probability of retrieved cloud state C from a set of satellite observed features F. Features F can for instance be continuous cloud mask scores like the $\mathrm{B_{score}}$ or the $\mathrm{T_{score}}$ (see Section 4.1). $P(C)$ is the prior probability of observed cloud state C. Observations in this context are "reference" observations of the "true" cloud state. $P(F|C)$ is the conditional probability of features F given observed cloud state C. The denominator

$$P(F) = P(C)P(F|C) + P(\bar{C})P(F|\bar{C}) \tag{41}$$

is a normalizing factor which gives the overall probability of features F for cloudy C and cloud free $\bar{C}$ observations. C and $\bar{C}$ are pre-calculated by counting cloudy and cloud free observations and by calculating the respective occurrence probability. $P(F|C)$ and $P(F|\bar{C})$ are pre-calculated by counting the co-occurrence of features F with associated cloud state C and $\bar{C}$ and calculating the respective conditional co-occurrence probabilities. In order to calculate $P(F|C)$, the value range of F has to be discretized into M bins and the N features have to be related to each other. The conditional probabilities $P(F|C)$ and $P(F|\bar{C})$ can then be calculated by counting the number of cloudy observation C and cloud free observations $\bar{C}$ that fall into each of the M bins of each of the N features. With the full implementation of the Bayes theorem the conditional probability $P(F|C)$ would be a M^N histogram. This full implementation is often not feasible due to the lack of a sufficient number of observations. With $M = 35$ and $N = 5$ the conditional probability $P(F|C)$ is a 5 dimensional histogram where each dimension has 35 bins. This yields more than $50 \cdot 10^6$ histogram bins. In order to fill these bins $\gg 100$ observations per histogram bin are required and not every histogram bin is equally covered in the observational space. The often chosen naïve Bayesian approach circumvents this problem by assuming features to be independent of each other. The one dimensional histograms are calculated per feature, which requires less observations. The implementation of the naïve Bayesian cloud mask approach can be solved with a multiplicative treatment of conditional

probabilities:

$$P(C|F) = \frac{P(C)\prod_{i=1}^{N} P(F_i|C)}{P(F)}, \tag{42}$$

where

$$P(F) = P(C)\prod_{i=1}^{N} P(F_i|C) + P(\bar{C})\prod_{i=1}^{N} P(F_i|\bar{C}). \tag{43}$$

6.2 Implementation

A Bayesian classifier for cloud detection can be based on the "classical" cloud mask tests (see e.g. Heidinger et al. (2012)) with the benefit of retrieving a continuous cloud state probability together with the cloud state itself. The implementation chosen here however differs from the often chosen naïve Bayesian classifier approach in the following ways:

1. A subset of the continuous cloud mask scores (features) from Section 4.1 are employed to estimate Cloud Amount (CA) and Cloud Fractional Cover (CFC) instead of a binary cloud / cloud free state mask.
2. Co-variability of continuous cloud mask scores (features) is exploited by choice of two dimensional instead of one dimensional feature histograms.

The first choice is based on the insight that cloud cover observations are not binary. The binary cloud / clear separation is a highly artificial choice which can be made more or less cloud conservative in dependence of the envisioned application of the cloud mask. This decision is optimally made by the user and not by the producer of the cloud mask. CA has a finite number O of CA classes (i.e. the SYNOP okta classes) and CFC is a continuous measure of cloud cover. These two measures are much more appropriate to describe cloud state for downstream applications than a binary cloud mask.

The second choice is based on the insight that some features F_i are not stand-alone cloud state predictors like needed for the naïve Bayesian approach. This limitation can be demonstrated with the two features $\mathrm{B}_{\mathrm{score}}$ and $\mathrm{STR}_{\mathrm{score}}$. The $\mathrm{B}_{\mathrm{score}}$ is a good stand-alone predictor of cloud state. A cloud is mostly brighter than the underlying surface (except for instance over snow or desert). The $\mathrm{STR}_{\mathrm{score}}$ is not a stand-alone predictor of cloud state. It is high for scattered low cumulus over the ocean, but it is low for both clear sky or stratus clouds. The latter ones have a low spatio-temporal variability which yields a low $\mathrm{STR}_{\mathrm{score}}$. When treating the $\mathrm{B}_{\mathrm{score}}$ and the $\mathrm{STR}_{\mathrm{score}}$ as independent features in a naïve Bayesian classifier, the separation of clear sky and cloudy cases would become "fuzzier" compared to the use of the $\mathrm{B}_{\mathrm{score}}$ alone.

The $\mathrm{STR}_{\mathrm{score}}$ can only be used conditionally together with other features in order to be useful. The added value of the $\mathrm{STR}_{\mathrm{score}}$ is for instance the detection of scattered and/or moving cumulus with a low instantaneous spectral footprint in the solar or thermal channels, but it cannot decide between completely cloud free (0-1 okta) or completely cloudy (7-8 okta) situations. In order to exploit the added value of a feature like the $\mathrm{STR}_{\mathrm{score}}$ two dimensional feature histograms always combine the

co-variability of a state score and a variability score. With more spectral information such as available for MSG SEVIRI the co-variability could also be calculated from two state scores. The use of co-variability in a Bayesian cloud classifier guarantees that a large part of the score inter-dependence is explicitly resolved with the benefit of requiring only M^2 histogram bins instead of M^N histogram bins as in the full Bayesian solution. The implementation is as follows:

$$P(C_o|F) = \frac{P(C_o)\prod_{\substack{i=1\\j=1}}^{N/2} P(F_i,F_j|C_o)}{P(F)}, \tag{44}$$

where

$$P(F) = \sum_{o=1}^{O}\left[P(C_o)\prod_{\substack{i=1\\j=1}}^{N/2} P(F_i,F_j|C_o)\right], \tag{45}$$

with $o = 1..O$ being the observation classes. The product has to be calculated with only half of the features $N/2$ since two features are used per conditional probability histogram $P(F_i,F_j|C_o)$. $i = 1..N/2$ and $j = 1..N/2$ are the two features i and j assigned to each conditional histogram. The normalizing denominator is summed over all observation classes and conditional histograms.

The two dimensional histograms implemented in the Bayesian cloud classifier of GeoSatClim are listed in Table 6. Only two histograms and only two dimensional histograms are implemented since neither the additional use of single dimensional feature histograms nor the additional use of other two dimensional histograms (e.g. combining the VIS and IR state features) did show better performance in CFC estimation. The possible benefit of a combined use of the 6.2 μm water vapor channel (available for MFG MVIRI and most older GEO sensors) with e.g. the 10.8 μm window channel in a two dimensional histogram has yet to be explored (A. Heidinger, personal communication). The CFC detection during night using this set-up is limited to a single two dimensional histogram combining the $\mathrm{T}_{\mathrm{score}}$ and the $\mathrm{TV}_{\mathrm{score}}$.

Table 6: The two dimensional feature histograms selected for the Bayesian classifier.

Histogram No.	Feature F_1	Feature F_2
1	$\mathrm{B}_{\mathrm{score}}$	$\mathrm{STR}_{\mathrm{score}}$
2	$\mathrm{T}_{\mathrm{score}}$	$\mathrm{TV}_{\mathrm{score}}$

6.3 Observational Constraint

Synoptic cloud observations (SYNOP) with a range of 0–8 (oktas) are used as observational constraint. According to the observational guide of the World Meteorological Organization (2008) 0 okta means completely cloud free and 8 okta means completely overcast. The word “completely” has a strong implication on the measurement of CA: a single cloud or a single cloud gap yields 1 okta and 7 okta respectively. In the range of 2–6 okta CA is linearly related to CFC. In accordance with Reuter et al. (2009) 0 and 1 okta classes are joined here to a single 1 okta class and 7 and 8 okta are joined to a single 7 okta class. This yields $O = 7$ classes. The CA histogram shown in Figure 9 has a “U”

shape where completely cloudy and cloud free cases dominate over partial cloudiness classes. So around 30% are fully cloud free (≤ 1 okta), around 30% are fully cloudy (≥ 7 okta) and 30% have an intermediate cloud state ($2 - 6$ okta).

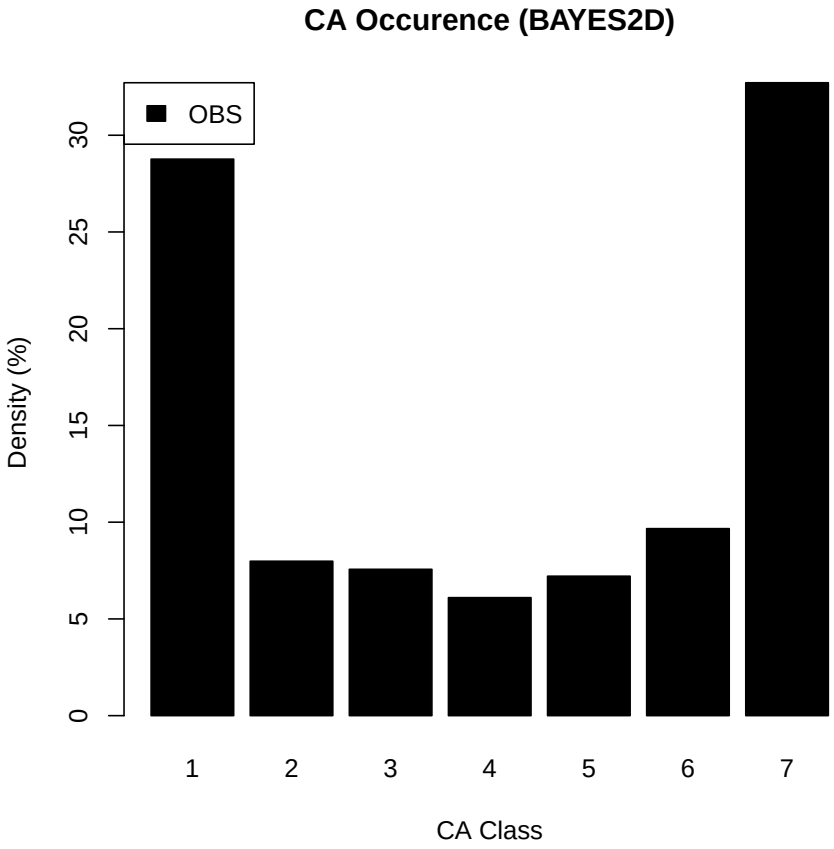

Figure 9: Prior probability of cloud occurrence on the Meteosat Disc binned by cloud amount (CA) class.

Separate training of the Bayesian cloud classifier is performed for each sensor. Spectral characteristics slightly differ between MFG and MSG and the different measurement interval leads to different temporal variability. The period 2000–2005 is chosen for MFG and 2004–2009 is chosen for MSG. The initial ECMWF archive contains data for over 6000 globally distributed sites. From these we selected sites for a geographic range of 60° N to 60° S and 60° W to 60° E, and for which the satellite viewing angle is below 70° . In order to ensure the collection of long-term homogenous data series, we selected stations where observations were continuously performed for the training period 2000–2009, at least every 6 hours with a maximum break of 30 days. For each site we used cloud amount observed with the highest temporal frequency (up to 1 hour) that was reported for the whole 25-year period. Thus the frequency of observations could vary between sites, but remained stable in time for each site. Further, we excluded sites for which the Standard Normal Homogeneity Test (SNHT, see Section G.3 for details) detected any inhomogeneity in a time series of cloud amount monthly anomalies.

Since SYNOP reporting WMO stations are unevenly distributed in geographic space (Figure 10 left panel), a regular grid spacing is created. For each 2° x 2° geographic grid cell the SYNOP site

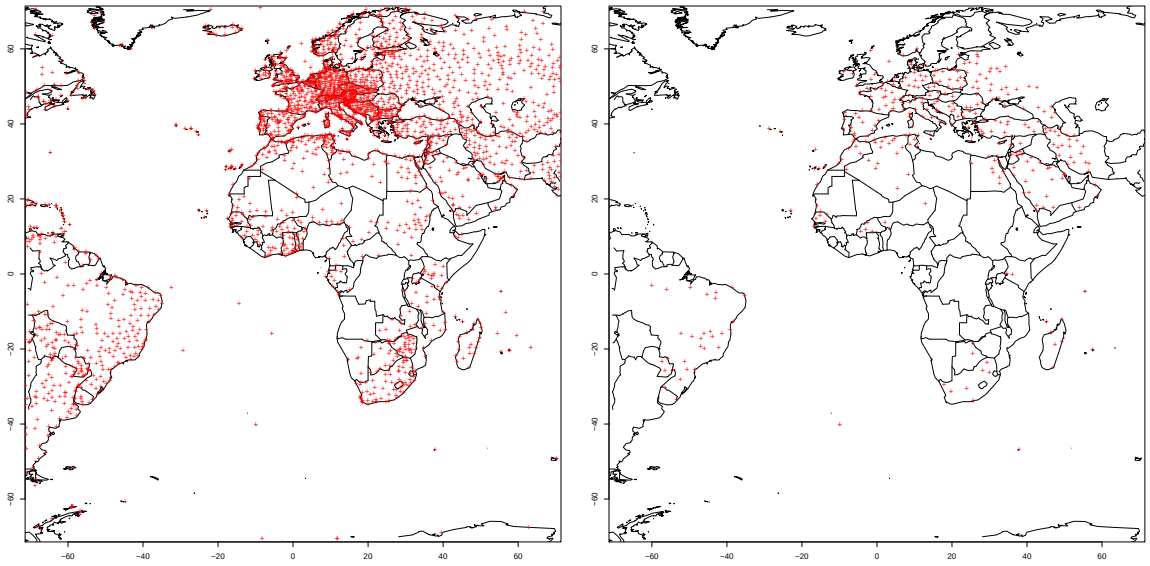

Figure 10: Left: all quality screened SYNOP reporting WMO sites. Right: same as left, but gridded to a 2° x 2° geographic grid.

with the most valid observations is used. This yields a total of 339 WMO sites distributed over the full Meteosat disc (Figure 10 right panel). The Meteosat pixel closest to the site is selected. Since SYNOP is irregularly spaced in time (either 3 or 6 hourly observation interval, often with missing observations) collocation in time is performed as follows: in order to minimize the impact of time difference between satellite and ground observed CA on skill scores the satellite-based feature closest to the observational time is chosen (Bojanowski et al., 2014). SYNOP observations further include implicit (but unquantified) observational averaging with a time span of up to one hour: it would need to be carefully evaluated as a next step if averaging satellite observations would further increase comparability.

6.4 Conditional Probabilities

The prior probability by CA class o is calculated as follows:

$$P(C_o) = \frac{\sum \mathrm{CA}(o)}{\sum \mathrm{CA}}, \tag{46}$$

where $\sum \mathrm{CA}(o)$ is the total amount of SYNOP CA observations with class o and $\sum \mathrm{CA}$ is the total amount of SYNOP CA observations (covering all classes). The resulting histogram of all CA classes is shown in Figure 9.

Continuous Features are discretized with $M = 35$ histogram bins. The bins $1..M$ are evenly distributed within the 1% and 99% percentile range of the feature distribution covering all chosen SYNOP sites. The conditional probability for the two dimensional histogram with bin index k of

feature i and bin index l of feature j is calculated by observation class o:

$$P(F_i(k), F_j(l)|C_o) = \frac{\sum(\mathrm{CA}(o), F_i(k), F_j(l))}{\sum \mathrm{CA}(o)}, \tag{47}$$

where $\sum(\mathrm{CA}(o), F_i(k), F_j(l))$ counts all SYNOP CA observations with class o which fall in bin k of the first feature F_i and simultaneously fall in bin l of the second feature F_j. This yields O two dimensional conditional histograms $P(F_i, F_j|C_o)$ for each set of two dimensional features.

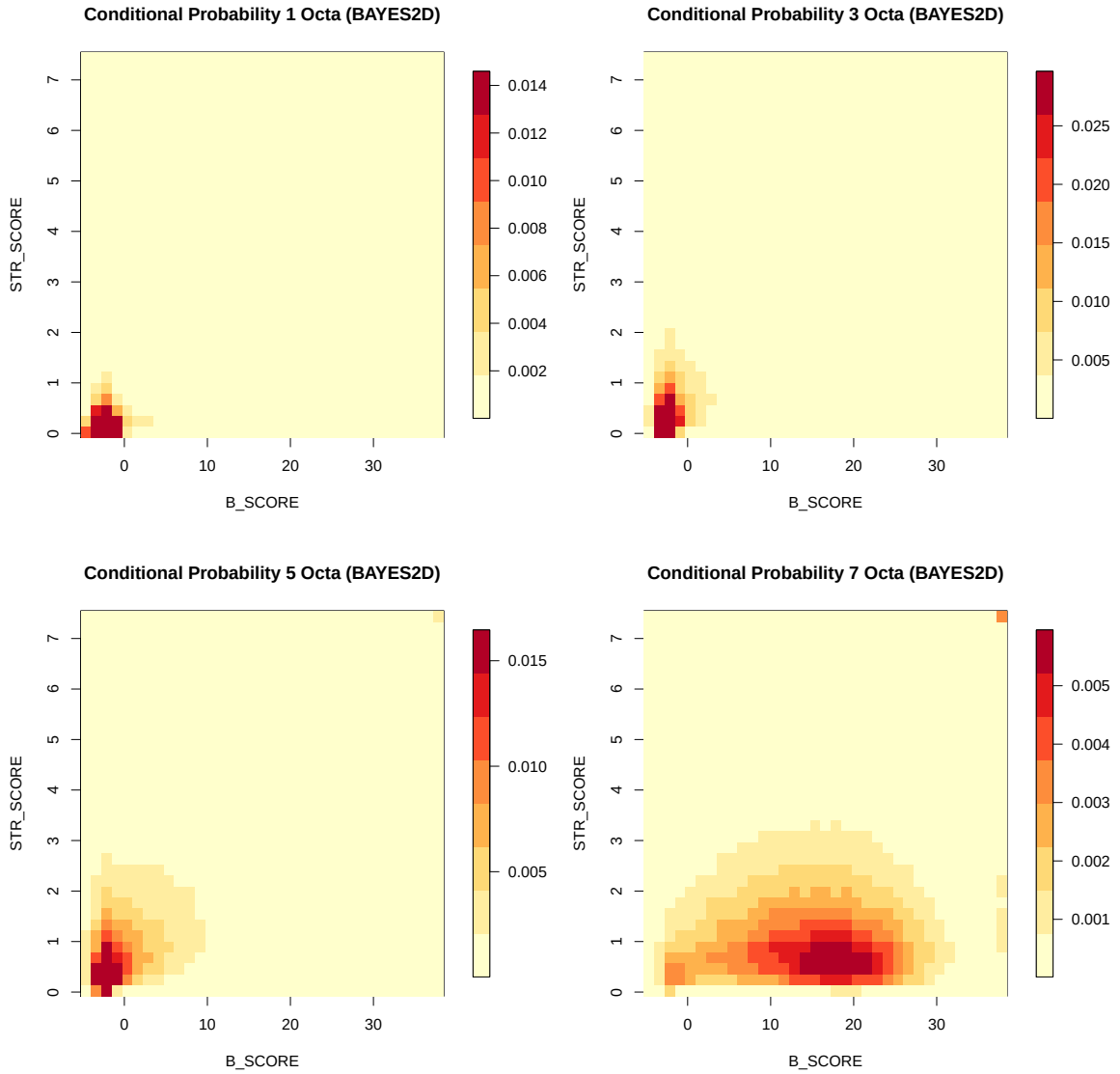

Figure 11: Conditional probability of cloud occurrence in dependence of the Brightness Score $\mathrm{B_{score}}$ and the Spatio-Temporal Reflectance Variance Score $\mathrm{STR_{score}}$ on the Meteosat Disc for cloud amount (CA) classes 1, 3, 5 and 7. Conditional proababilities add up to unity for each CA class.

Two examples for these two dimensional histograms are given in Figures 11 and 12. Figure 11 visualizes the relationship of the Brightness Score $\mathrm{B_{score}}$ on the horizontal axis to the Spatio-Temporal Reflectance Variance Score $\mathrm{STR_{score}}$ on the vertical axis for different CA classes. These histograms firstly demonstrate that the two scores are not independent. There is added information by jointly

analyzing them: e.g. the conditional probability for the 7 okta class is highest for the $\mathrm{B}_{\mathrm{score}} \approx 18$, but only when the $\mathrm{STR}_{\mathrm{score}} \approx 0.5$. So, the cloud detection capability of the $\mathrm{B}_{\mathrm{score}}$ co-varies with the value of the $\mathrm{STR}_{\mathrm{score}}$. This result justifies the choice of two dimensional instead of independent one-dimensional histograms. Secondly, by use of Bayes and two dimensional histograms it is possible to not just discriminate cloudy and non-cloudy situations but the full range of 7 okta classes. Both Figures also demonstrate that there is substantial information hidden in the two heritage Meteosat channels (the visible and the infrared channel) which can be statistically related to cloud amount. The two Figures however indicate that there is still room for improvement: that the histogram bins could still be optimized: the upper bounds for both the state and the variability score are almost empty. The choice of the 99% percentile may be relaxed to e.g. the 95% percentile upper bound in a next version in order to better exploit the lower histogram range where cloud detection occurs. The 1% percentile for the lower bound is justified for both the state and variability scores.

6.5 Calculation of CA and CFC

In order to resolve all 7 okta classes the following classification is chosen derive CA from $P(C_o|F)$:

1. CA=1 when $P(C_{o=1}|F) \geq P_{\mathrm{min}}$, else
2. CA=7 when $P(C_{o=7}|F) \geq P_{\mathrm{min}}$, else
3. CA=o with o the class of maximum probability $\max\left(P(C_o|F)\right)$.

where $P_{\mathrm{min}} = 50\%$ is the minimum per class probability required to identify fully cloud free and fully cloud cover situations. This threshold would be subject to tuning, but was set to 50% in order to be compatible with the binary classification used elsewhere. With this threshold the above discrimination of course simplifies to the last term since a probability of $\geq 50\%$ always identifies the class with the maximum probability. The associated probability $P(\mathrm{CA})$ is then set to $P(C_o|F)$ where o is the CA class.

CFC is associated to CA after the World Meteorological Organization (2008) with minor modifications for the 0/1 and 7/8 okta classes (Table 7).

Table 7: Relationship of cloud amount (CA) to cloud fractional cover (CFC).

Class	CA (WMO) okta	CA okta	CFC %
1	0 and 1	1	0
2	2	2	25
3	3	3	40
4	4	4	50
5	5	5	60
6	6	6	75
7	7 and 8	7	100

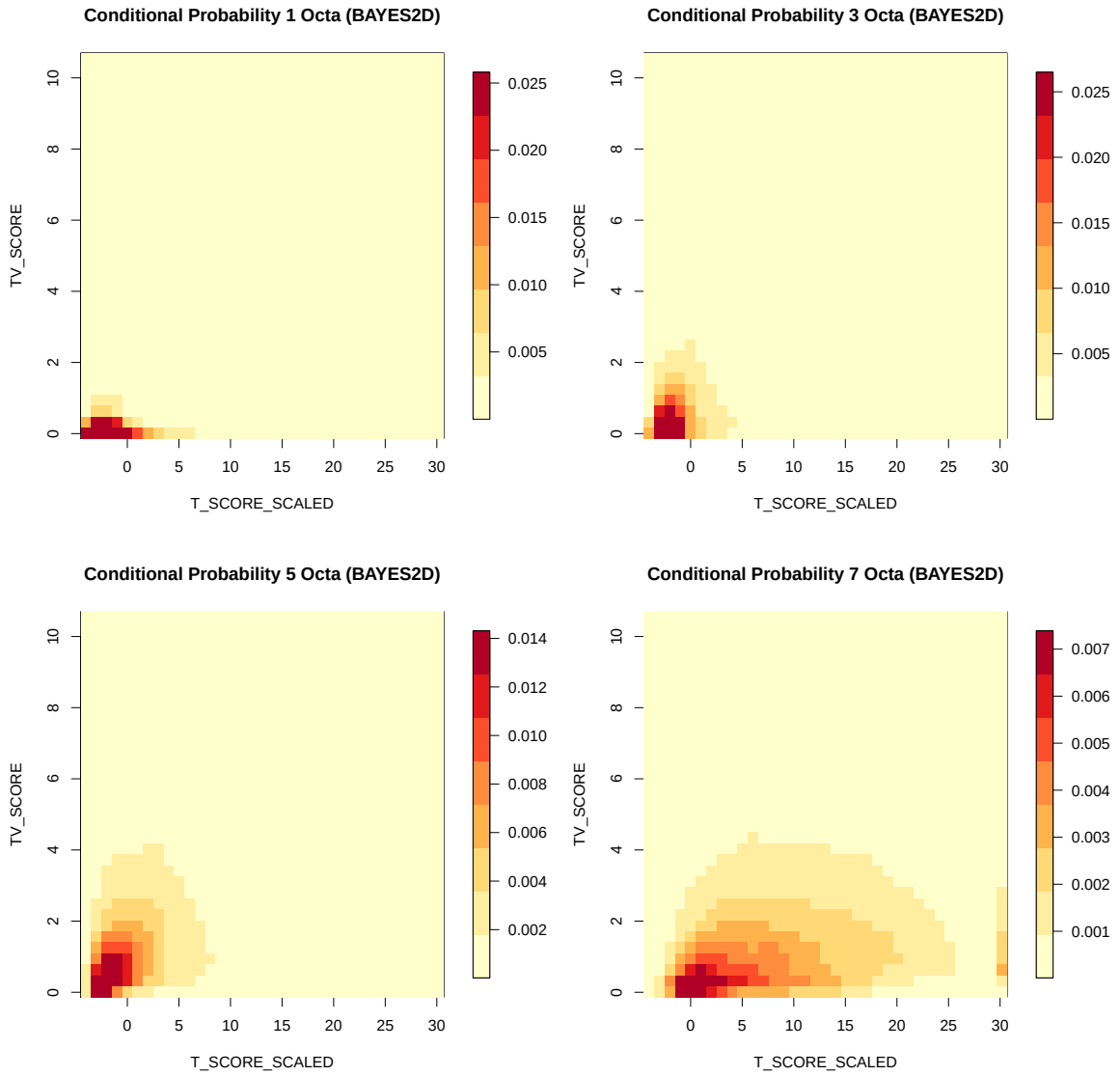

Figure 12: Conditional probability of cloud occurrence in dependence of both the Temperature Score $\mathrm{T}_{\mathrm{score}}$ and the Temporal Temperature Variance Score $\mathrm{TV}_{\mathrm{score}}$ on the Meteosat Disc for cloud amount (CA) classes 1, 3, 5 and 7.

6.6 Evaluation of CA and CFC

A short evaluation of the algorithm performance carried out during the algorithm development is presented here. It is based on a single year 2005. The full validation with independent ground and satellite-based observational datasets is presented in the validation report [RD 3].

6.6.1 Instantaneous Skill Scores

Instantaneous binary skill scores are calculated by assigning 0,1 okta classes to 0 and 7,8 okta classes to 1. Intermediate 2–6 okta classes are omitted. The two employed skill scores are: the Hansen Kuiper's skill score (HK) and the bias score (Wilks, 2011):

$$\mathrm{HK} = \frac{ad - bc}{(a+c)(b+d)} \tag{48}$$

$$\text{bias score} = \frac{a+b}{a+c}, \tag{49}$$

where a (correct detections), b (false alarms), c (misses) and d (correct no-detection) count the different cases of satellite-based cloud cover versus reference observations in the form of a contingency matrix. A perfect cloud detection yields a HK of one, random retrieval yields a HK of zero, and inferior to random yields a negative HK. The bias score is one if the number of satellite-observed cloud detections corresponds to the number of SYNOP-observed cloud detections (unbiased prediction). It is lower than one if the satellite observes more cloud free cases during SYNOP-observed cloud cases (overprediction), and it is higher than one for exaggerated satellite-observed cloudiness (underprediction).

The regularly spaced SYNOP sites used for training in Section 6.3 are chosen for the algorithm evaluation. Sites with a HK< 0.6 are discarded since visual inspection gave a strong indication of SYNOP observation artifacts (e.g. CA always at 0 or 8 okta). An independent set of SYNOP sites is going to be selected for validation as part of the validation report and SYNOP screening is going to be based on multiple independent satellite-based CA/CFC estimates.

The mean HK is 0.913 for MFG MVIRI and 0.931 for MSG SEVIRI. The mean bias score is 0.997 for MFG MVIRI and 1.008 for MSG SEVIRI. The instantaneous binary skill score statistics however strongly depend on sun and satellite view zenith angle. These dependencies are displayed in Figure 13 and Figure 14 for MFG MVIRI and MSG SEVIRI. Boxes in both figures denote 1st and 3rd quartiles and the thick horizontal line marks the median value. Whiskers indicate largest and lowest values within 1.5 times the interquartile range, while circles represent values beyond this range. During daylight ($\theta_s < 90°$) the cloud detection for both sensor generations features a HK> 0.9. HK decreases to around 0.8 during night time when the state and variability of only a single thermal channel can be used in the Bayesian classifier. During night time the bias score is higher than 1, corresponding to an overestimation of cloudy cases.

The sensitivity of cloud detection to the satellite view zenith angle is shown in the right panels of Figure 13 and Figure 14. HK is above 0.8 for most sites, but the spread increases with decreasing

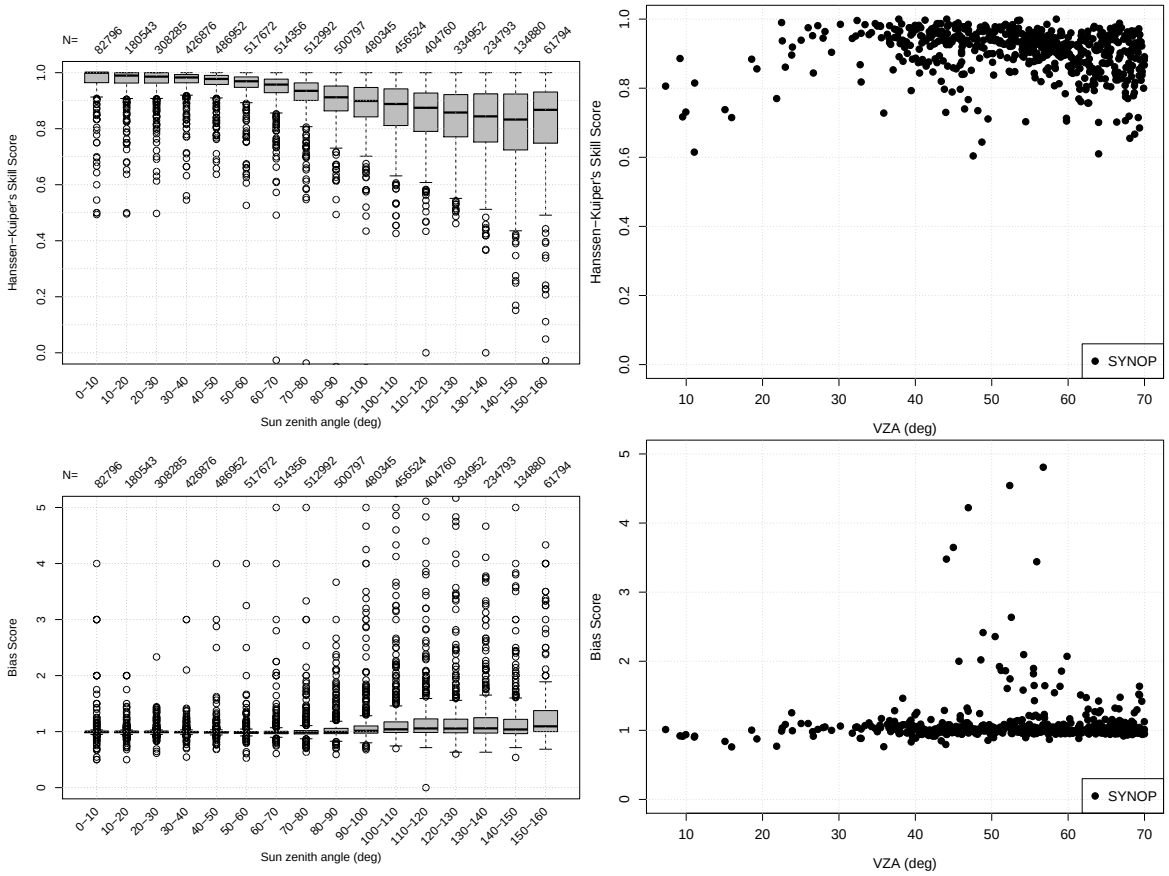

Figure 13: Instantaneous binary skill score statistics of the MFG MVIRI-based CA during 2005 based on 565 SYNOP sites: Hansen-Kuiper's skill score (HK) vs. sun and satellite view zenith angle (upper left and right) and bias score vs. sun and satellite view zenith angle (lower left and right).

HK at higher θ_v. A few outliers with HK< 0.8 yield a very high positive bias score independent of satellite view zenith angle. Further investigation and inter-comparison during the validation phase with other satellite-based CA datasets will show whether these sites are subject to additional SYNOP quality issues and potentially need to be omitted.

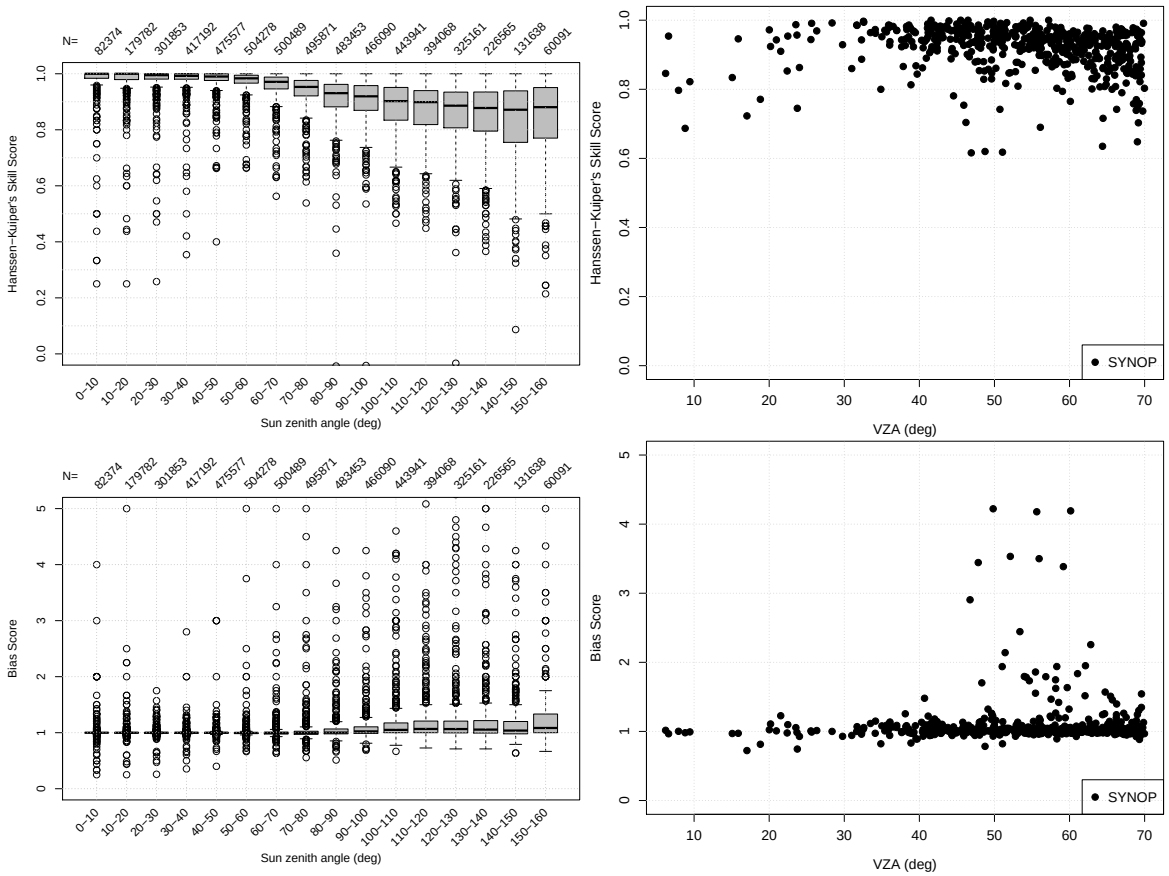

Figure 14: Instantaneous binary skill score statistics of the MSG SEVIRI-based CA during 2005 based on 556 SYNOP sites: Hansen-Kuiper's skill score (HK) vs. sun and satellite view zenith angle (upper left and right) and bias score vs. sun and satellite view zenith angle (lower left and right).

6.6.2 Daily and Monthly Mean Accuracy

The accuracy requirements for the MVIRI / SEVIRI CFC TCDR defined by CM SAF specify a maximum bias (mean bias error MBE, positive or negative) of 0.1 (threshold), 0.05 (target) and 0.01 (optimal). The maximum bias-corrected root mean square error (bcRMSE) is specified as 0.35 (threshold), 0.30 (target) and 0.25 (optimal) for daily mean CFC and 0.25 (threshold), 0.20 (target) and 0.15 (optimal) for monthly mean CFC. These accuracy requirements are absolute requirements for CFC ranging from 0.0–1.0 (0–100% cloud fractional cover). These accuracy requirements are averaged quantities covering the full processing area. They are calculated as the mean CFC accuracy for the equally spaced 2° x 2° SYNOP sites distributed over the full Meteosat disc. The SYNOP sites were assigned to one of the five broad global climate zones (arid, cold, tropical, temperate and polar) of the Köppen classification (Köppen, 1936) available as an updated geographical map of 0.1° x 0.1° resolution (Peel et al., 2007). Sites which could not be assigned to a land point were labeled as “ocean”.

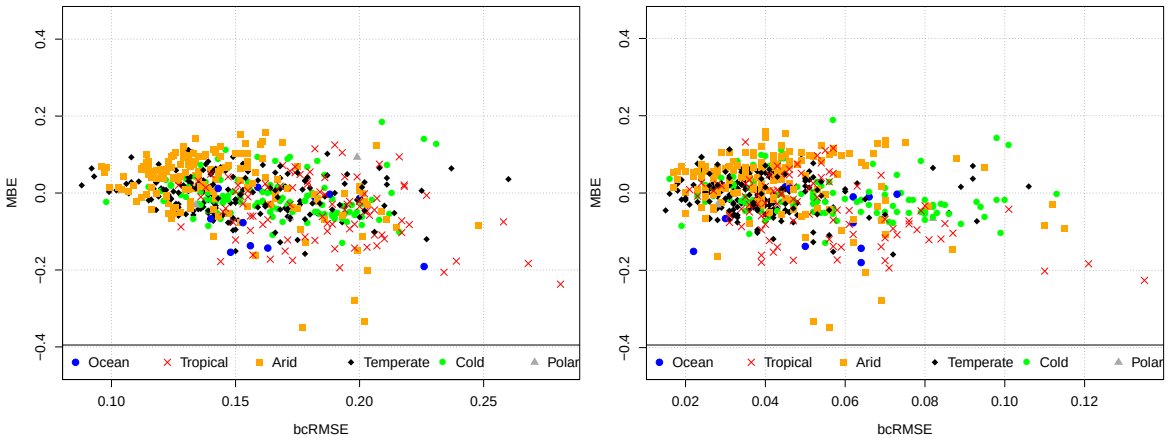

Figure 15: Hourly (left) and monthly (right) continuous statistics of the MFG MVIRI-based CFC during 2005 based on 565 SYNOP sites.

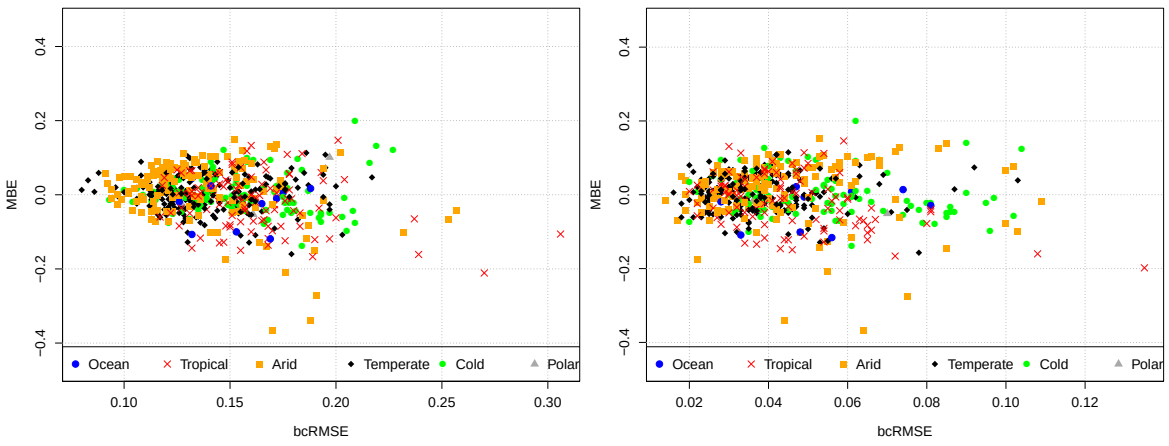

Figure 16: Hourly (left) and monthly (right) continuous statistics of the MSG SEVIRI-based CFC during 2005 based on 556 SYNOP sites.

The resulting MBE for the single year 2005 is -0.005 (MFG MVIRI) and 0.001 (MSG SEVIRI) and

thus fulfills the optimal requirement for the chosen evaluation year. The daily mean bcRMSE is 0.175 (MFG MVIRI) and 0.162 (MSG SEVIRI). The monthly mean bcRMSE is 0.086 (MFG MVIRI) and 0.081 (MSG SEVIRI). Both daily and monthly mean fulfill the optimal accuracy requirement for the evaluated year. The analysis of the final full 30+ year long time series will possibly yield higher uncertainties due to larger radiometric calibration and geometric registration uncertainties of earlier MVIRI sensors on board Meteosat 2-6. The analysis of the full time series will also allow to quantify whether the decadal stability requirements are fulfilled.

The continuous daily and monthly mean statistics for individual SYNOP sites are displayed in Figure 15 for MFG MVIRI and in Figure 16 for MSG SEVIRI. They reveal a substantial site-to-site variability of both the MBE and bcRMSE which not visible from the averaged quantities. SYNOP sites in cold and temperate climate zones are generally within a MBE of -0.2 to 0.2, so individual sites will not meet the bias requirement. They however most meet the daily and monthly bcRMSE requirement. A few tropical sites have a higher bcRMSE > 0.2 for daily means and > 0.1 for monthly means. A few arid sites underestimate CFC by more than 20% (MBE < -0.2), which needs a closer analysis also with respect to the quality of the underlying SYNOP data.

The left panel of Figure 15 shows that MFG MVIRI has a higher spread than MSG SEVIRI. For MFG MVIRI the station bias becomes negative with increasing bcRMSE. This in turn suggests that there is potential to train the Bayesian classifier (which was trained only with MSG SEVIRI data) separately with MFG MVIRI data.

7 Spatial and Temporal Aggregation

All variables are spatially aggregated to the geographic projection with a regular grid space of 0.05° x 0.05° covering the geographic range of 65° N to 65° S and 65° W to 65° E by use of a maximum $\theta_{\mathrm{v}} = 60°$.

Hourly means are the mean of all valid instantaneous retrievals for a given hour. As an example:

- MFG: the 0 hour mean is composed of 2 full disc scans starting at 0 and 30 minutes after 00:00 UTC
- MSG: the 0 hour mean is composed of 4 full disc scans starting at 0, 15, 30 and 45 minutes after 00:00 UTC

The hourly mean is calculated if a single hourly retrieval is present. The daily mean is the mean of all hourly means if at least four hourly means are present. The monthly mean is the mean of all daily means if at least 20 valid daily means are present. The monthly mean diurnal cycle is a vector of 24 values containing the mean hourly values for the respective month for hours with at least 20 valid hourly means.

The temporal aggregation of continuous variables such as the CFC or the $\mathrm{TV}_{\mathrm{score}}$ is carried out by calculating the arithmetic mean value. No weighting is applied. The temporal aggregation of non-continuous (e.g. classified) variables such as CM or CA is carried out by calculating the median value.

8 Directions for Future Improvements

8.1 General

1. The cloud mask CM is associated with an ad-hoc uncertainty CM^{σ}: by use of the Bayesian classifier a true uncertainty could be calculated. This would imply that the Bayesian concept would already be applied as part of the CM calculation. In the current formulation the CM and the CM scores are calculated first without using the Bayesian classifier. The scores are then used to calculate the conditional probability histograms for the Bayesian classifier. Using the Bayesian concept directly to calculate CM and the scores would require to solve the classical "chicken and egg" problem: no Bayesian classifier without a pre-calculated score, but no pre-calculated score without a Bayesian classifier. An iterative approach may be tested.
2. The Bayesian classifier uses two dimensional score dependencies where the inter-dependence of a state score and a variability score are exploited. The inter-dependence of scores like the brightness and the temperature score is currently not exploited. The benefit of multi-dimensional bayesian histograms (e.g. three to five dimensional) for CA and CFC retrieval should further be tested. With limited spectral coverage from old GEO sensors no information should be discarded even if only of limited additional use. The possible benefit of a combined

use of the 6.2 μm water vapor channel (available for MFG MVIRI and most older GEO sensors) with e.g. the 10.8 μm window channel in a two dimensional histogram has yet to be explored (A. Heidinger, personal communication).

3. The optimal estimation approach using Radiative Transfer Model (RTM) inversion is among the newest generation of cloud retrieval schemes not included nor reviewed here. It might be explored how such physically consistent solutions can be applied to heritage sensors with missing spectral resolution. This would imply to apply the optimal estimation approach not just to minimize the cost function across channels but also in time (and space), and by possibly constraining the RTM with self-contained clear sky boundary fields as presented in this report.

4. The algorithms could be extended to include other geostationary sensors such as GOES or GMS with a similar spectral coverage to MFG. It would need to be tested whether SRF differences would imply a sensor-by-sensor set of conditional probabilities for the Bayesian CA and CFC classifier or whether a normalization of spectral radiances to a common SRF is applicable. The current retrieval of CM, CA and CFC does further not make use of the WV channel of geostationary sensors. It should be exploited if the full set of 3 channels (VIS, WV and IR) can be used to improve a generalized cloud mask, cloud amount and cloud fraction retrieval from geostationary sensors.

5. GeoSatClim is used to derive downstream variables LST and FTH. Since pre- and post-processing is a substantial part of the computational overhead when building satellite-based TCDR's it would be wise to include other physical variables such as the full surface radiation balance or other land surface and atmospheric state variables as part of GeoSatClim . Apart from performance such an extension would also increase consistency across ECV's since in a single processing scheme they all make use of exactly the same radiance processing, clear sky filtering and static as well as dynamic boundary conditions.

6. GeoSatClim is currently applicable to geostationary sensors only. This scope is justified for equatorial regions with a low view zenith angle and it is justified for the high temporal resolution offered by these sensors. A joint retrieval using co-located radiances from polar orbiting sensors at higher latitudes could be envisioned. These sensors (AVHRR, HIRS, AMSU, SSM/I) offer an extended spectral coverage in the visible, near-infrared, infrared and microwave spectrum. They would allow a dynamic (scene-by-scene) training of the three heritage channel radiances of geostationary sensors for the retrieval of currently unexploited ECV's such as cloud physical parameters like cloud optical thickness, cloud water path, clear sky atmospheric parameters such as aerosol optical depth or land surface parameters like leaf area index and surface albedo. Such a strategy of joining radiances is more difficult than the often used posteriori combination of geostationary and polar orbiting TCDR's but has the benefit of maximizing the use of available information by combining spectral resolution of polar orbiting with temporal resolution geostationary sensors.

8.2 Detailed

- The initial ToA BT from ECMWF is simulated by use of an ad-hoc correction for water vapor and θ_v. The inversion of the LST algorithm (retrieving ToA BT from LST) might be a better choice.

- MSG SEVIRI radiances use standard calibration factors from EUMETSAT. A small improvement can be expected by utilizing inter-calibration factors provided by EUMETSAT through the

Global Space-based Inter-Calibration System (GSICS) project. Explore whether the use of GSICS inter-calibration factors yield better CM, CA and CFC (and downstream variables like LST or FTH)

- The temporal smoothing of MFG MVIRI inter-calibration factors fails for abrupt gain changes. A break detection and piece-wise smoothing has to be implemented
- Build on MFG VIS radiances for the MFG MVIRI sensor which include spectral aging (Decoster, 2013) instead of the operational stable target linear degradation (Govaerts et al., 2004).
- The linear approximation for building a broad band VIS channel from the two narrow-band VIS channels presented in Section 3.5 is a valid approach for separating cloudy from non-cloudy reflectances when the background reflectance is subtracted prior to classification. A more complex approach for narrow-to-broadband conversion, such as using a combined atmosphere and canopy radiative transfer model or a scene-dependent formulation, would be required to represent the diverse spectral footprints of the underlying land and ocean surface for retrieving land or ocean physical parameters.

9 Glossary

ATBD	Algorithm Theoretical Basis Document
AVHRR	Advanced Very High Resolution Radiometer (NOAA/Metop)
BIL	Bilinear
BRDF	Bidirectional Reflectance Distribution Function
BSRN	Baseline Surface Radiation Network
BT	Brightness Temperature
CA	Cloud Amount
CDOP	Continuous Development and Operations Phase
CFC	Cloud Fractional Cover
CGIAR	Consultative Group on International Agricultural Research
CM	Cloud Mask
CM SAF	Satellite Application Facility on Climate Monitoring
CGMS	Coordination Group for Meteorological Satellites
COSMO	Consortium for Small-scale Modeling
CTH	Cloud Top Height
CTP	Cloud Top Pressure
DN	Digital Number
DWD	German Weather Service
ECEF	Earth-Centered Earth-Fixed coordinate system
ECMWF	European Centre for Medium-Range Weather Forecasts
ECV	Essential Climate Variables
EUMETSAT	European Organisation for the Exploitation of Meteorological Satellites
FCDR	Fundamental Climate Data Record (e.g. calibrated radiances)
FAR	False Alarm Rate
GCOS	Global Climate Observing System
GMS	Geostationary Meteorological Satellite (Japan)
GOES	Geostationary Operational Environmental Satellite (USA)
GSHHS	Global, Self-consistent, Hierarchical, High-resolution Shoreline
GSICS	Global Space-based Inter-Calibration System (CGMS/WMO)
HIRS	High Resolution Infrared Radiation Sounder (on NOAA POES platforms)
HK	Hansen Kuipers Discriminant
HR	Hit Rate
HRV	SEVIRI High Resolution Visible Channel
IR	Infrared
MBE	Mean Bias Error
MFG	Meteosat First Generation
MSG	Meteosat Second Generation
MVIRI	Meteosat Visible and Infrared Imager (MFG)
NASA	National Aeronautics and Space Administration (USA)
NIR	Near Infrared
NN	Nearest Neighbor
NOAA	National Oceanic and Atmospheric Administration (USA)
NWP	Numerical Weather Prediction
NWP SAF	Satellite Application Facility for Numerical Weather Prediction
POD	Probability of Detection
RMSE	Root Mean Square Error
RTM	Radiative Transfer Model

SAF	Satellite Application Facility
SCOPE-CM	Sustained COordinated Processing of Environmental satellite data for Climate Monitoring
SEVIRI	Spinning Enhanced Visible and Infrared Imager (MSG)
SPARC	Separation of Pixels using an Aggregated Rating over Canada
SSP	Sub-Satellite Point
SRTM	Shuttle Radar Topography Mission
TCDR	Thematic Climate Data Record (e.g. physical quantities)
ToA	Top of Atmosphere
UTC	Universal Time Coordinate
VIS	Visible
VISSN	MVIRI visible channel
WMO	World Meteorological Organization
WV	Water Vapor

10 References

References

Alexandersson, H. (1986). A homogeneity test applied to precipitation data. *J. Climatol.*, 6(6):661–675.

Berendes, T., Kuo, K., Logar, A., Corwin, E., Welch, R., Baum, B., Pretre, A., and Weger, R. (1999). A comparison of paired histogram, maximum likelihood, class elimination, and neural network approaches for daylight global cloud classification using avhrr imagery. *Journal of Geophysical Research-Atmospheres*, 104(D6):6199–6213.

Berrisford, P., Dee, D., Fielding, K., Fuentes, M., Kallberg, P., Kobayashi, S., and Uppala, S. (2009). The era-interim archive version 1.0. ERA Report Series 1, ECMWF, European Centre for Medium Range Weather Forecasts Shinfield Park, Reading, Berkshire RG2 9AX, United Kingdom.

Bojanowski, J., Stöckli, R., Tetzlaff, A., and Kunz, H. (2014). The impact of time difference between satellite overpass and ground observation on cloud cover performance statistics. *Remote Sens.*, 6:12866–12884.

Coordination Group for Meteorological Satellites (1999). LRIT/HRIT global specification. Technical Report CGMS 03, Issue 2.6, CGMS Secretariat EUMETSAT, Am Kavalleriesand 31, P.O.Box 100555, D-64205 Darmstadt, Germany.

Decoster, I. (2013). *Spectral ageing model for the Meteosat First Generation visible band*. PhD thesis, Vrije Universiteit Brussel, Faculty of Engineering Sciences, Department of Electronics and Informatics.

Decoster, I., Clerbaux, N., Baudrez, E., Dewitte, S., Ipe, A., Nevens, S., Blazquez, A. V., and Cornelis, J. (2013a). A spectral aging model for the meteosat-7 visible band. *Journal of Atmospheric and Oceanic Technology*, 30:496–509.

Decoster, I., Clerbaux, N., Baudrez, E., Dewitte, S., Ipe, A., Nevens, S., Blazquez, A. V., and Cornelis, J. (2014). Spectral aging model applied to meteosat first generation visible band. *Remote Sensing*, 6:2534–2571.

Decoster, I., Clerbaux, N., Govaerts, Y. M., Baudrez, E., Ipe, A., Dewitte, S., Nevens, S., Blazquez, A. V., and Cornelis, J. (2013b). Evidence of pre-launch characterization problem of meteosat-7 visible spectral response. *Remote Sensing Letters*, 4(10):1008–1017.

Dee, D. P., Uppala, S. M., Simmons, A. J., Berrisford, P., Poli, P., Kobayashi, S., Andrae, U., Balmaseda, M. A., Balsamo, G., Bauer, P., Bechtold, P., Beljaars, A. C. M., van de Berg, L., Bidlot, J., Bormann, N., Delsol, C., Dragani, R., Fuentes, M., Geer, A. J., Haimberger, L., Healy, S. B., Hersbach, H., Holm, E. V., Isaksen, L., Kallberg, P., Kohler, M., Matricardi, M., McNally, A. P., Monge-Sanz, B. M., Morcrette, J.-J., Park, B.-K., Peubey, C., de Rosnay, P., Tavolato, C., Thepaut, J.-N., and Vitart, F. (2011). The era-interim reanalysis: configuration and performance of the data assimilation system. *Q. J. R. Meteorol. Soc.*, 137:553–597.

Deneke, H. M. and Roebeling, R. A. (2010). Downscaling of meteosat seviri 0.6 and 0.8 mu m channel radiances utilizing the high-resolution visible channel. *Atmospheric Chemistry and Physics*, 10(20):9761–9772.

Duan, S.-B., Li, Z.-L., Wang, N., Wu, H., and Tang, B.-H. (2012). Evaluation of six land-surface diurnal temperature cycle models using clear-sky in situ and satellite data. *Rem. Sens. Environ.*, 124:15–25.

Duan, S.-B. y., Li, Z.-L., Wu, H., Tang, B.-H., Jiang, X., and Zhou, G. (2013). Modeling of day-to-day temporal progression of clear-sky land surface temperature. *IEEE Geosci. Remote Sens. Lett.*, 10(5):1050–1054.

Dürr, B., Schröder, M., Stöckli, R., and Posselt, R. (2013). Heliofth: combining cloud index principles and aggregated rating for cloud masking using infrared observations from geostationary satellites. *Atmos. Meas. Tech.*, 6:1883–1901.

Dybbroe, A., Karlsson, K., and Thoss, A. (2005). Nwcsaf avhrr cloud detection and analysis using dynamic thresholds and radiative transfer modeling. part i: Algorithm description. *Journal of Applied Meteorology*, 44(1):39–54.

EUMETSAT (2005). 0 degree operational service meteosat-7 calibration report issue 30. Technical Report EUM/OPS/REP/05/1938, EUMETSAT, EUMETSAT, Am Kavalleriesand 31, D-64295 Darmstadt, Germany.

EUMETSAT (2010). Meteosat VIS channel calibration information. PDF-TEN-VIS-CHANNEL-CALIB, EUMETSAT, EUMETSAT, Am Kavalleriesand 31, D-64295 Darmstadt, Germany.

EUMETSAT (2011). Meteosat first generation user handbook. Technical Report EUM/OPS/USR/10/1537, issue v1A, EUMETSAT Eumetsat-Allee 1, D-64295 Darmstadt, Germany.

EUMETSAT (2012). The conversion from effective radiances to equivalent brightness temperatures. Technical Report EUM/MET/TEN/11/0569, EUMETSAT Am Kavalleriesand 31, D-64295 Darmstadt, Germany.

Fontana, F., Stöckli, R., and Wunderle, S. (2010). Evaluation of a probabilistic cloud masking algorithm for climate data record processing: Sparc: a new scene identification algorithm for msg seviri. Visiting Scientist Report 14, EUMETSAT Satellite Application Facility on Climate Monitoring.

Gieske, A., Hendrikse, J., Retsios, V., van Leeuwen, B., Maathuis, B., Romaguera, M., Sobrino, J., Timmermans, W., and Su, Z. (2005). Processing of msg - 1 seviri data in the thermal infrared - algorithm development with the use of the sparc2004 data set. In *Proceedings of the ESA WPP-250, SPARC final workshop, 4-5 July, 2005. Enschede : ESA, 2005.*, 8 pp.

Göttsche, F. and Olesen, F. (2009). Modelling the effect of optical thickness on diurnal cycles of land surface temperature. *Remote Sensing of Environment*, 113(11):2306–2316.

Govaerts, Y., Clerici, M., and Clerbaux, N. (2004). Operational calibration of the meteosat radiometer vis band. *Ieee Transactions On Geoscience and Remote Sensing*, 42(9):1900–1914.

Haimberger, L. (2007). Homogenization of radiosonde temperature time series using innovation statistics. *J. Clim.*, 20(7):1377–1403.

Heidinger, A. K., Evan, A. T., Foster, M. J., and Walther, A. (2012). A Naive Bayesian Cloud-Detection Scheme Derived from CALIPSO and Applied within PATMOS-x. *Journal of Applied Meteorology and Climatology*, 51:1129–1144.

Hollstein, A., Fischer, J., Henken, C. C., and Preusker, R. (2014). Bayesian cloud detection for meris, aatsr, and their combination. *Atmos. Meas. Tech. Discuss.*, 7:11045–11085.

John, V. O., Tabata, T., Ruethrich, F., Roebeling, R. A., Hewison, T., and Schulz, J. (2019). On the recalibration of infrared (ir) and water vapour (wv) radiance time-series from european and japanese geostationary satellites. *Submitted to Remote Sensing*.

Karlsson, K.-G., Johansson, E., and Devasthale, A. (2015). Advancing the uncertainty characterisation of cloud masking in passive satellite imagery: Probabilistic formulations for noaa avhrr data. *Remote Sens. Environ.*, 158:126–139.

Khaliq, M. and Ouarda, T. (2007). On the critical values of the standard normal homogeneity test (SNHT). *Int. J. Climatol.*, 27:681–687.

Khlopenkov, K. V. and Trishchenko, A. P. (2007). Sparc: New cloud, snow, and cloud shadow detection scheme for historical 1-km avhhr data over canada. *J Atmos Oceanic Tech*, 24(3):322–343.

Köppen, W. (1936). *Das geographische System der Klimate.*, volume 5. Gebrüder Bornträger, Berlin.

Kriebel, K., Gesell, G., Kastner, M., and Mannstein, H. (2003). The cloud analysis tool apollo: improvements and validations. *International Journal of Remote Sensing*, 24:2389–2408.

Kurucz, R. (1992). Synthetic infrared spectra. In Rabin, D. and Jefferies, J., editors, *Proceedings of the 154th Symposium of the International Astronomical Union (IAU), Tucson, Arizona, March 2–6, 1992*, Infrared Solar Physics, Norwell, MA. KLUWER ACADEMIC PUBL.

Mannstein, H., Broesamle, H., Schillings, C., and Trieb, F. (1999). Using a meteosat cloud index to model the performance of solar thermal power stations. In *The 1999 EUMETSAT Meteorological Satellite Data Users' Conference, 6-10 September 1999*, volume EUM P 26, pages 239–246, Copenhagen, Denmark. EUMETSAT.

Mayer, B. and Kylling, A. (2005). Technical note: The libradtran software package for radiative transfer calculations - description and examples of use. *Atmospheric Chemistry and Physics*, 5:1855–1877.

Meyer, P., Itten, K. I., Kellenberger, T., Sandmeier, S., and Sandmeier, R. (1993). Radiometric corrections of topographically induced effects on landsat tm data in an alpine environment. *ISPRS-J. Photogramm. Remote Sens.*, 48(4):17–28.

Müller, R., Dagestad, K., Ineichen, P., Schroedter-Homscheidt, M., Cros, S., Dumortier, D., Kuhlemann, R., Olseth, J., Piernavieja, G., Reise, C., Wald, L., and Heinemann, D. (2004). Rethinking satellite-based solar irradiance modelling – the solis clear-sky module. *Remote Sensing of Environment*, 91(2):160–174.

Peel, M. C., Finlayson, B. L., and McMahon, T. A. (2007). Updated world map of the koppen-geiger climate classification. *Hydrol. Earth Syst. Sci.*, 11(5):1633–1644.

Rahman, H., Pinty, B., and Verstraete, M. M. (1993). Coupled surface-atmosphere reflectance (csar) model .2. semiempirical surface model usable with NOAA advanced very high-resolution radiometer data. *J. Geophys. Res.-Atmos.*, 98(D11):20791–20801.

Reuter, M., Thomas, W., Albert, P., Lockhoff, M., Weber, R., Karlsson, K. G., and Fischer, J. (2009). The cm-saf and fub cloud detection schemes for seviri: Validation with synoptic data and initial comparison with modis and calipso. *Journal of Applied Meteorology and Climatology*, 48(2):301–316.

SAFNWC (2013). Algorithm theoretical basis document for cloud products. Algorithm Theoretical Basis Document SAF/NWC/CDOP2/MFL/SCI/ATBD/01, Issue 3, Rev. 2.1, Satellite Application Facility on Support to Nowcasting and Very Short Range Forecasting.

Schaaf, C. B., Gao, F., Strahler, A. H., Lucht, W., Li, X. W., Tsang, T., Strugnell, N. C., Zhang, X. Y., Jin, Y. F., Muller, J. P., Lewis, P., Barnsley, M., Hobson, P., Disney, M., Roberts, G., Dunderdale, M., Doll, C., d'Entremont, R. P., Hu, B. X., Liang, S. L., Privette, J. L., and Roy, D. (2002). First operational BRDF, albedo nadir reflectance products from modis. *Remote Sens. Environ.*, 83:135–148.

Schmetz, J., Pili, P., Tjemkes, S., Just, D., Kerkmann, J., Rota, S., and Ratier, A. (2002). An introduction to meteosat second generation (msg). *B Am Meteorol Soc*, 83(7):977–992.

Stephens, L. G. (1994). *Remote Sensing of the Lower Atmosphere*. Oxford University Press, 523 pp.

Stöckli, R. (2013). The HelioMont Surface Solar Radiation Processing. Scientific Report 93, MeteoSwiss, 122 pp.

Swisstopo (2005). Approximate solution for the transformation ch1903 - wgs84. Technical report, Bundesamt für Landestopografie swisstopo.

Tan, B., Wolfe, R., Masek, J., Gao, F., and Vermote, E. F. (2010). An illumination correction algorithm on landsat-tm data. In *Geoscience and Remote Sensing Symposium (IGARSS)*, pages 1964–1967. IEEE International.

USGS (1996). GTOPO30. Digital Media.

Vemury, S., Stowe, L. L., and Anne, V. R. (2001). Avhrr pixel level clear-sky classification using dynamic thresholds (clavr-3). *J. Atmospheric Oceanic Technology*, 18(2):169–186.

Vollmer, M. and Gedzelmann, S. (2006). Colours of the sun and moon: the role of the optical air mass. *European Journal of Physics*, 27:299–309.

Wessel, P. and Smith, W. (1996). A global, self-consistent, hierarchical, high-resolution shoreline database. *Journal of Geophysical Research-Solid Earth*, 101(B4):8741–8743.

Wilks, D. (2011). *Statistical Methods in the Atmospheric Sciences*. International Geophysics. Academic Press, 704 pp.

World Meteorological Organization (2008). Guide to meteorological instruments and methods of observation. Technical Report WMO-No. 8, Seventh Edition, World Meteorological Organization.

Zelenka, A., Perez, R., Seals, R., and Renne, D. (1999). Effective accuracy of satellite-derived hourly irradiances. *Theor Appl Climatol*, 62(3-4):199–207.

A Sensor Parameters

A.1 Spectral Response Function

The original normalized spectral response function $\xi(\lambda)$ by satellite and sensor are used as available from EUMETSAT (Table 9).

Table 9: Reference to the documents containing sensor-specific spectral response functions

Satellite	Sensor	No.	Document	Document Date
MFG	MVIRI	1	PDF_TEN_SPECTR-RESP-MET-1.pdf	25.04.2014
MFG	MVIRI	2	PDF_TEN_SPECTR-RESP-MET-2.pdf	25.04.2014
MFG	MVIRI	3	PDF_TEN_SPECTR-RESP-MET-3.pdf	25.04.2014
MFG	MVIRI	4	PDF_TEN_SPECTR-RESP-MET-4.pdf	25.04.2014
MFG	MVIRI	5	PDF_TEN_SPECTR-RESP-MET-5.pdf	25.04.2014
MFG	MVIRI	6	PDF_TEN_SPECTR-RESP-MET-6.pdf	25.04.2014
MFG	MVIRI	7	PDF_TEN_SPECTR-RESP-MET-7.pdf	25.04.2014
MSG	SEVIRI	1–4	MSG_SEVIRI_Spectral_Response_Characterisation.XLS	30.10.2012

EUMETSAT suggests to use the MFG 7 VIS channel SRF for MFG 5 and MFG 6 (EUMETSAT, 2010). Other studies find a poorly characterized SRF of MFG 7 (Decoster et al., 2013b) and suggest to use the SRF of the MSG1 HRV channel. Until these questions have been properly answered, the original SRF will be used in GeoSatClim .

A.2 Central Wavelength

The nominal central wavelength λ_0 (μ m) is given by EUMETSAT from sensor specification (EUMETSAT, 2011; Schmetz et al., 2002). The nominal central wavenumber $\nu_0 = 10000/\lambda_0$ (cm^{-1}) can be converted from the central wavelength. The actual central wavelength is a SRF-weighted sum over the wavelength range:

$$\lambda_0^a = \frac{\sum_\lambda \xi(\lambda)\lambda}{\sum_\lambda \xi(\lambda)}, \tag{50}$$

or as central wavenumber:

$$\nu_0^a = \frac{\sum_\nu \xi(\nu)\nu}{\sum_\nu \xi(\nu)}. \tag{51}$$

A.3 Bandwidth

The nominal bandwidth $\Delta\lambda_0$ (μ m) is given by EUMETSAT from sensor specification (EUMETSAT, 2011; Schmetz et al., 2002). The nominal bandwidth as wavenumber $\Delta\nu_0$ (cm^{-1}) cannot be simply

converted from the nominal bandwidth as wavelength. The actual bandwidth is a SRF-weighted sum over the wavelength range:

$$\Delta\lambda_0^a = \sum_\lambda \xi(\lambda)\Delta\lambda, \tag{52}$$

or as the bandwidth as wavenumber:

$$\Delta\nu_0^a = \sum_\nu \xi(\nu)\Delta\nu, \tag{53}$$

where the integration is best performed by using $\pm 0.5\Delta\lambda$ or $\pm 0.5\Delta\nu$centered on the discretized SRF grid in the respective wavelength or wavenumber units.

A.4 Spectral Solar Irradiance

Channel integrated solar irradiance R_s (W m^{-2}) is derived by use of the spectral solar irradiance $R_\mathrm{s}(\lambda)$ (mW m^{-2} nm^{-1}) data by Kurucz (1992) resampled to 1 nm wavelength as part of the libRadtran software package (Mayer and Kylling, 2005):

$$R_\mathrm{s} = \sum_\lambda \frac{R_\mathrm{s}}{1000}(\lambda)\xi(\lambda)\Delta\lambda, \tag{54}$$

where the integration is performed over the SRF $\xi(\lambda)$ linearly interpolated to the $R_\mathrm{s}(\lambda)$ spectral discretization with $\Delta\lambda = 1$ nm. In case the spectral solar irradiance R_s^ν (mW m^{-2} (cm^{-1})$^{-1}$) is needed per wavenumber, the channel integrated solar irradiance can be converted as follows:

$$R_\mathrm{s}^\nu = \frac{R_\mathrm{s}\lambda_0^2}{10\Delta\lambda_0^a}, \tag{55}$$

where λ_0 (μm) is the nominal center wavelength and $\Delta\lambda_0^a$ (μm) is the actual bandwidth of the respective satellite channel.

B Time

Time t (h) is given as fractional hours with reference to UTC and marks the start of the scan or aggregation period of each instantaneous retrieval or aggregation. The fractional day of year is calculated as follows from the day of year DoY:

$$D = \mathrm{DoY} - 1 + \frac{t + t_\mathrm{scan}(l)}{24}, \tag{56}$$

where $t_\mathrm{scan}(l)$ (h) is the scan time for image line l since the start of the scan. The scan time is approximated with the following formula for all geostationary sensors:

$$t_{\text{full}} = \frac{n_l}{60 n_s \text{rpm}} \tag{57}$$

$$t_{\text{scan}}(l) = t_{\text{full}} \frac{l + 0.5\left(n_l - n_l^{\text{visible}}\right) - 1}{n_l}, \tag{58}$$

where t_{full} (h) is the full time for a scan (approximately 12.5 minutes for MSG SEVIRI or 25 minutes for MFG MVIRI), rpm is the sensor rotation per minute (100 for both MSG SEVIRI and MFG MVIRI), n_l is the total number of lines (3750 for MSG SEVIRI and 5000 for MFG MVIRI), n_s is the number of lines per scan step (3 for MSG SEVIRI and 1 for MFG MVIRI) and n_l^{visible} is the number of visible lines out of the n_l total lines (3712 for MSG SEVIRI and 5000 for MFG MVIRI).

The number of days for year Y. $n_{\text{DoY}} = 365$ days for regular and $n_{\text{DoY}} = 366$ days for leap years. Leap years are detected by use of the Gregorian calendar:

$$\text{leap year} = (((Y\%4) = 0) \text{ and } ((Y\%100) \neq 0)) \text{ or } ((Y\%400) = 0). \tag{59}$$

The Julian Day JD is the fractional day number since January 1, 4713 BC (not to be confused with the day of year DoY):

$$\text{JD} = K - 32075 + 1461 \frac{Y + 4800 + \frac{M-14}{12}}{4} + 367 \frac{M - 2 - \frac{M-14}{12} \cdot 12}{12} - 3 \frac{\frac{Y+4900+\frac{M-14}{12}}{100}}{4}, \tag{60}$$

where M is the month of year (1..12) and K is the day of month (1..31) and all calculations of above equation have to be carried out as integer operations. This formula might be revised to calculate the true JD, which is a fractional JD given in days since January 1, 4713 BC 12 UTC.

C Angles

C.1 Sun Angles

The relative sun-earth distance in AU is calculated after World Meteorological Organization (2008). The formulas are given here for completeness:

$$d_{\text{s}} = 1.00014 - 0.01671 \cos g - 0.00014 \cos 2g \tag{61}$$

$$g = 357.528 + 0.9856003 n, \text{ where } 0 \leq g < 360, \tag{62}$$

and where $n = \text{JD} - 2451545.0$ and JD is the Julian Day (see Appendix B).

Sun zenith θ_{s} and azimuth ϕ_{s} angles are calculated for each satellite pixel and at each time step. For a given date, the equation of time ET (minutes) and the earth's declination with respect to the orbital plane δ_s (degrees) can be approximated by:

Table 10: Empirical coefficients needed to calculate the equation of time and declination

No.	e	d
1	229.18	0.006918
2	0.000075	0.399912
3	0.001868	0.070257
4	0.032077	0.006758
5	0.014615	0.000907
6	0.040849	0.002697
7	-	0.00148

$$\mathrm{ET} = e_1(e_2 + e_3\cos\gamma - e_4\sin\gamma - e_5\cos 2\gamma - e_6\sin 2\gamma) \quad (63)$$

$$\delta_\mathrm{s} = d_1 - d_2\cos\gamma + d_3\sin\gamma - d_4\cos 2\gamma + d_5\sin 2\gamma - d_6\cos 3\gamma + d_7\sin 3\gamma \quad (64)$$

where $\gamma = 2\pi D/365$ is the fractional year (radians) for the fractional day of year D (see Appendix B). The fourier series coefficients e and d are given in Table 10. The true solar time (TST, minutes) can be calculated from the universal time coordinate (UTC, minutes) for longitude λ:

$$\mathrm{TST} = \mathrm{UTC} + \mathrm{ET} + 4\lambda \quad (65)$$

The hour angle HA (radians) is then:

$$\mathrm{HA} = \frac{\pi}{180}\left(\frac{\mathrm{TST}}{4} - 180\right), \quad (66)$$

which allows the calculation of the sun zenith angle θ_s:

$$\theta_\mathrm{s} = \arccos\left(\min(\max(\sin\phi\sin\delta_\mathrm{s} + \cos\phi\cos\delta_\mathrm{s}\cos\mathrm{HA}, -1), 1)\right) \quad (67)$$

and the sun azimuth angle ϕ_s:

$$\phi_\mathrm{s} = \arccos\left(\min(\max(\frac{-(\sin\phi\cos\theta_\mathrm{s} - \sin\delta_\mathrm{s})}{\cos\phi\sin\theta_\mathrm{s}}, -1), 1)\right) \quad (68)$$

where ϕ_s with $\mathrm{TST} > 720$ minutes is converted from the range $-180^\circ \ldots 0^\circ$ to $180^\circ \ldots 360^\circ$. This conversion is required because ϕ_s is defined clock-wise with 0° pointing towards North, 90° East, 180° South and 270° West.

C.2 Satellite Angles

The satellite view zenith angle θ_v and view azimuth angle ϕ_v are calculated for each satellite pixel. They give the view geometry of the observer at the center of the pixel in the direction of the satellite sensor. For geostationary satellite platforms these angles could be handled as static fields. However, during the operation period the satellite position and thus the sub-satellite point (SSP) can drift by as much as 1° . This requires the constant re-adjustment of the satellite view angles. Also, two redundant operational geostationary satellites are often located at slightly different orbital positions. They provide imagery in alternating mode in order to guarantee a continuous data stream

even during times when one instrument performs maintenance. For instance, the MSG sub-satellite longitude is known to vary between -3.4° East and 10° East.

First, the geocentric latitudes of the observer ϕ'_{obs} and the satellite instrument ϕ'_{sat} are calculated from their geographic (geodetic, corresponding to the WGS84 ellipsoid) latitudes ϕ_{obs} and ϕ_{sat}:

$$\phi' = \arctan\left[\tan(\phi)\,(1-f)^2\right], \tag{69}$$

where

$$f = \frac{R_{\mathrm{E}} - R_{\mathrm{P}}}{R_{\mathrm{E}}} \tag{70}$$

is the earth's flattening, and where ϕ_{obs} corresponds to the pixel's center latitude ϕ and the equatorial and polar earth radius R_{E} (m) and R_{P} (m) are defined as given in Coordination Group for Meteorological Satellites (1999). Geocentric longitude exactly corresponds to geographic (geodetic) longitude. Next the observer height in relation to the earth's center is calculated from the observer latitude:

$$H_{\mathrm{obs}} = R_{\mathrm{E}}\left(1 - \frac{e^2 s^2}{2} + \frac{e^4 s^2}{2} - \frac{5e^4 s^4}{8}\right) + z_{\mathrm{obs}}, \tag{71}$$

where

$$e = \frac{\sqrt{R_{\mathrm{E}}^2 - R_{\mathrm{P}}^2}}{R_{\mathrm{E}}} \tag{72}$$

$$s = \sin\phi_{\mathrm{obs}}, \tag{73}$$

where e is the earth's eccentricity and z_{obs} (m) is the elevation of the observer, corresponding to the pixel's center elevation z. The geodetic observer and satellite coordinates are then transformed into earth-centered earth-fixed (ECEF) coordinates including their vector norms:

$$X_{\mathrm{obs}} = H_{\mathrm{obs}} \cos\phi'_{\mathrm{obs}} \cos\lambda_{\mathrm{obs}} \tag{74}$$

$$Y_{\mathrm{obs}} = H_{\mathrm{obs}} \cos\phi'_{\mathrm{obs}} \sin\lambda_{\mathrm{obs}} \tag{75}$$

$$Z_{\mathrm{obs}} = H_{\mathrm{obs}} \sin\phi'_{\mathrm{obs}} \tag{76}$$

$$N_{\mathrm{obs}} = \sqrt{X_{\mathrm{obs}}^2 + Y_{\mathrm{obs}}^2 + Z_{\mathrm{obs}}^2} \tag{77}$$

$$X_{\mathrm{sat}} = H_{\mathrm{sat}} \cos\phi'_{\mathrm{sat}} \cos\lambda_{\mathrm{sat}} \tag{78}$$

$$Y_{\mathrm{sat}} = H_{\mathrm{sat}} \cos\phi'_{\mathrm{sat}} \sin\lambda_{\mathrm{sat}} \tag{79}$$

$$Z_{\mathrm{sat}} = H_{\mathrm{sat}} \sin\phi'_{\mathrm{sat}} \tag{80}$$

$$N_{\mathrm{sat}} = \sqrt{X_{\mathrm{sat}}^2 + Y_{\mathrm{sat}}^2 + Z_{\mathrm{sat}}^2}. \tag{81}$$

For the observer location, the ECEF coordinates need to first be transformed to the components of the vector which is normal on the to the surface of the earth's geoid:

$$X'_{\rm obs} = Z_{\rm obs}\frac{\cos\lambda_{\rm obs}}{\tan\phi_{\rm obs}} \quad (82)$$

$$Y'_{\rm obs} = Z_{\rm obs}\frac{\sin\lambda_{\rm obs}}{\tan\phi_{\rm obs}} \quad (83)$$

$$Z'_{\rm obs} = Z_{\rm obs} \quad (84)$$

$$N'_{\rm obs} = \sqrt{(X'_{\rm obs})^2 + (Y'_{\rm obs})^2 + (Z'_{\rm obs})^2}, \quad (85)$$

and

$$N_{\rm sat-obs} = \sqrt{(X_{\rm sat} - X_{\rm obs})^2 + (Y_{\rm sat} - Y_{\rm obs})^2 + (Z_{\rm sat} - Z_{\rm obs})^2}. \quad (86)$$

The geocentric angle between the direction of the satellite and the observer is:

$$\delta_{\rm sat-obs} = \arccos\left(\frac{X_{\rm sat}X_{\rm obs} + Y_{\rm sat}Y_{\rm obs} + Z_{\rm sat} - Z_{\rm obs}}{N_{\rm sat}H_{\rm obs}}\right) \quad (87)$$

The satellite view zenith angle can then be calculated as:

$$\theta_{\rm v} = \arccos\left(\frac{X_{\rm obs}(X_{\rm sat} - X_{\rm obs}) + Y_{\rm obs}(Y_{\rm sat} - Y_{\rm obs}) + Z_{\rm obs}(Z_{\rm sat} - Z_{\rm obs})}{H_{\rm obs}N_{\rm sat-obs}}\right) \quad (88)$$

In order to determine the view azimuth angle the vector V90 in the meridional plane perpendicular to the vertical of the observation point and pointing to the north pole is calculated:

$$X_{\rm V90} = -X'_{\rm obs}Z'_{\rm obs} \quad (89)$$

$$Y_{\rm V90} = -Y'_{\rm obs}Z'_{\rm obs} \quad (90)$$

$$Z_{\rm V90} = (X'_{\rm obs})^2 + (Y'_{\rm obs})^2 \quad (91)$$

$$N_{\rm V90} = \sqrt{X^2_{\rm V90} + Y^2_{\rm V90} + Z^2_{\rm V90}}. \quad (92)$$

The vector V0 orthogonal to V90 and the observation vector is formed (3 axis right-hand system with V0 pointing eastwards):

$$X_{\rm V0} = Y_{\rm V90}Z'_{\rm obs} - Z_{\rm V90}Y'_{\rm obs} \quad (93)$$

$$Y_{\rm V0} = Z_{\rm V90}X'_{\rm obs} - X_{\rm V90}Z'_{\rm obs} \quad (94)$$

$$Z_{\rm V0} = X_{\rm V90}Y'_{\rm obs} - Y_{\rm V90}X'_{\rm obs} \quad (95)$$

$$N_{\rm V0} = \sqrt{X^2_{\rm V0} + Y^2_{\rm V0} + Z^2_{\rm V0}}. \quad (96)$$

The vector SS pointing to the satellite from the observation point is calculated:

$$X_{\mathrm{SS}} = X_{\mathrm{sat}} - X_{\mathrm{obs}} \quad (97)$$
$$Y_{\mathrm{SS}} = Y_{\mathrm{sat}} - Y_{\mathrm{obs}} \quad (98)$$
$$Z_{\mathrm{SS}} = Z_{\mathrm{sat}} - Z_{\mathrm{obs}} \quad (99)$$
$$N_{\mathrm{SS}} = \sqrt{X_{\mathrm{SS}}^2 + Y_{\mathrm{SS}}^2 + Z_{\mathrm{SS}}^2}. \quad (100)$$

The vector on the tangent plane to the observation point and pointing to the satellite is calculated:

$$(Y'_{\mathrm{obs}} Z_{\mathrm{SS}} - Z'_{\mathrm{obs}} Y_{\mathrm{SS}}) \quad (101)$$
$$(Z'_{\mathrm{obs}} X_{\mathrm{SS}} - X'_{\mathrm{obs}} Z_{\mathrm{SS}}) \quad (102)$$
$$(X'_{\mathrm{obs}} Y_{\mathrm{SS}} - Y'_{\mathrm{obs}} X_{\mathrm{SS}}) \quad (103)$$

$$X_{\mathrm{P}} = Z'_{\mathrm{obs}}(Z'_{\mathrm{obs}} X_{\mathrm{SS}} - X'_{\mathrm{obs}} Z_{\mathrm{SS}}) - Y'_{\mathrm{obs}}(X'_{\mathrm{obs}} Y_{\mathrm{SS}} - Y'_{\mathrm{obs}} X_{\mathrm{SS}}) \quad (104)$$
$$Y_{\mathrm{P}} = X'_{\mathrm{obs}}(X'_{\mathrm{obs}} Y_{\mathrm{SS}} - Y'_{\mathrm{obs}} X_{\mathrm{SS}}) - Z'_{\mathrm{obs}}(Y'_{\mathrm{obs}} Z_{\mathrm{SS}} - Z'_{\mathrm{obs}} Y_{\mathrm{SS}}) \quad (105)$$
$$Z_{\mathrm{P}} = Y'_{\mathrm{obs}}(Y'_{\mathrm{obs}} Z_{\mathrm{SS}} - Z'_{\mathrm{obs}} Y_{\mathrm{SS}}) - X'_{\mathrm{obs}}(Z'_{\mathrm{obs}} X_{\mathrm{SS}} - X'_{\mathrm{obs}} Z_{\mathrm{SS}}) \quad (106)$$
$$N_{\mathrm{P}} = \sqrt{X_{\mathrm{P}}^2 + Y_{\mathrm{P}}^2 + Z_{\mathrm{P}}^2}. \quad (107)$$

The view azimuth angle is calculated as:

$$\phi_{\mathrm{v}} = \begin{cases} \alpha & \text{if } \beta \leq 90^\circ; \\ 360^\circ - \alpha & \text{if } \beta > 90^\circ \end{cases}, \quad (108)$$

where

$$\alpha = \arccos\left(\frac{X_{\mathrm{V90}} X_{\mathrm{P}} + Y_{\mathrm{V90}} Y_{\mathrm{P}} + Z_{\mathrm{V90}} Z_{\mathrm{P}}}{N_{\mathrm{V90}} N_{\mathrm{P}}}\right) \quad (109)$$
$$\beta = \arccos\left(\frac{X_{\mathrm{V0}} X_{\mathrm{P}} + Y_{\mathrm{V0}} Y_{\mathrm{P}} + Z_{\mathrm{V0}} Z_{\mathrm{P}}}{N_{\mathrm{V0}} N_{\mathrm{P}}}\right). \quad (110)$$

The above formulation has various limitations (polar areas, satellite vector pointing in the same direction as the observer vector) which have to be handled during the actual implementation. Gieske et al. (2005) point out to inaccuracies in the above formulation and suggest a simpler approach which should be carefully evaluated as a next step.

C.3 Sun-Satellite Angles

Radiative transfer model applications and empirical parameterizations of atmospheric or surface bidirectional reflectance require the specification of the relative sun – satellite view geometry. The

relative sun – satellite azimuth angle is calculated as follows:

$$\phi_{\mathrm{v-s}} = \phi_{\mathrm{v}} - \phi_{\mathrm{s}}, \tag{111}$$

where $\phi_{\mathrm{v-s}}$ is defined as 0° for the sun and the satellite located in the same direction and 180° for the sun and the satellite located opposite from each other. The radiative transfer model libRadtran for instance assumes $\phi_{\mathrm{v-s}}$ to be defined as 0° for the sun and the the satellite located opposite from each other. The definition of the relative sun – satellite azimuth angle can thus differ by 180° . While the satellite sensor azimuth angle is always defined with a clockwise rotation and 0° pointing North, the sun azimuth angle can also be defined as 0° pointing South with a clockwise (such as in libRadtran) or anti-clockwise rotation. In this document all azimuth angles are defined as 0° pointing North with a clockwise rotation.

The sun–satellite scattering angle is the relative angle enclosed by the two vectors pointing to the sun and the satellite. Here again, two definitions can be found in literature, and they are both used depending on the application. The backward scattering angle δ_{b} gives the amount of backward scattering and is often used in bidirectional reflectance calculations. It is at its maximum when the satellite is located in the direction of the sun:

$$\delta_{\mathrm{b}} = \arccos\left(\cos\theta_{\mathrm{v}}\cos\theta_{\mathrm{s}} + \sin\theta_{\mathrm{v}}\sin\theta_{\mathrm{s}}\cos\phi_{\mathrm{v-s}}\right). \tag{112}$$

The forward scattering angle δ_{f} gives the amount of forward scattering and is often used in specular reflection calculations (e.g. sun glint). It is at its maximum when the satellite is located opposite of the sun:

$$\delta_{\mathrm{f}} = \arccos\left(\cos\theta_{\mathrm{v}}\cos\theta_{\mathrm{s}} - \sin\theta_{\mathrm{v}}\sin\theta_{\mathrm{s}}\cos\phi_{\mathrm{v-s}}\right). \tag{113}$$

C.4 Terrain Angles

The clear sky reflectance on terrain is modeled in GeoSatClim ” by use of a pixel-wise local terrain aspect and slope. It can be calculated from the digital elevation model or estimated from the diurnal course of a cloud masked reflectance composite.

For terrain with tilt (slope) angle θ_{t} and azimuth (aspect) angle ϕ_{t} the angle between the sun direction and normal to the plane $\theta_{\mathrm{s-t}}$ is calculated,

$$\theta_{\mathrm{s-t}} = \arccos\left(\cos(\theta_{\mathrm{t}})\cos(\theta_{\mathrm{s}}) + \sin(\theta_{\mathrm{t}})\sin(\theta_{\mathrm{s}})\cos(\phi_{\mathrm{t}} - \phi_{\mathrm{s}})\right). \tag{114}$$

D Variability

D.1 Spatial Variability

The spatial variance of a pixel with location x, y within a two-dimensional array of size $n_x \times n_y$ is defined as the variance of all surrounding pixels within a circular distance of radius r:

$$\mathrm{VAR}_{x,y}(X) = \frac{1}{n} \sum_{i=x\pm\Delta x, j=y\pm\Delta y} (X_{i,j} - \bar{X})^2, \tag{115}$$

where $\Delta x = r$ and $\Delta y = r$ and where only surrounding pixels with $\sqrt{(i-x)^2 + (j-y)^2} \leq r$ are used in the summation. The spatial mean is:

$$\bar{X} = \frac{1}{n} \sum_{i=x\pm\Delta x, j=y\pm\Delta y} X_{i,j}. \tag{116}$$

Accordingly, the spatial standard deviation and the spatial difference can be calculated:

$$\sigma_{x,y}(X) = \sqrt{\frac{1}{n} \sum_{i=x\pm\Delta x, j=y\pm\Delta y} (X_{i,j} - \bar{X})^2} \tag{117}$$

$$\Delta_{x,y}(X) = \frac{1}{n} \sum_{i=x\pm\Delta x, j=y\pm\Delta y} X_{i,j} - X_{x,y}. \tag{118}$$

The spatial variability formulas in GeoSatClim are carried out with $r = 1$ or $r = 2$. Missing values are not summed and the sum is constrained to pixels within the bounds $n_x \times n_y$ (less values are summed at the grid boundaries).

D.2 Temporal Variability

The temporal variance of a pixel at time t is defined as:

$$\mathrm{VAR}_t(X) = \frac{1}{n} \sum_{s=t\pm\Delta t} (X_s - \bar{X})^2, \tag{119}$$

where the temporal mean is:

$$\bar{X} = \frac{1}{n} \sum_{s=t\pm\Delta t} X_s. \tag{120}$$

Accordingly, the temporal standard deviation can be calculated:

$$\sigma_t(X) = \sqrt{\frac{1}{n} \sum_{s=t\pm\Delta t} (X_s - \bar{X})^2} \tag{121}$$

The temporal variability formulas in GeoSatClim are carried out with $\Delta t = 4$ (MSG: ± 4 slots yield ± 1 hour temporal variability) or $\Delta t = 2$ (MFG: ± 2 slots yield ± 1 hour temporal variability). Missing values are not summed.

D.3 De-trended Temporal Variability

De-trended Temporal variability is required to separate the short term temporal fluctuations from a continuously rising/falling background signal (e.g. changing atmospheric brightness temperature from moving clouds versus changing radiative surface temperature from diurnal solar heating). De-trending is applied to a moving window of $t \pm \Delta t$ only if the Pearson correlation of the linear regression versus the original data is $r > 0.5$.

D.4 Spatio-Temporal Variability

Spatio-temporal variability is calculated by first calculating spatial variability and then calculating temporal variability of the spatial variability. This procedure can effectively remove background "clutter" not related to cloud forcing. While moving clouds over a homogeneous surface generate a similar signal in space and time, a land sea boundary generate a high spatial variability which is static in time. Such a static feature can be removed by calculating the temporal variability of the spatial variability.

E Boundary Conditions

E.1 Elevation

The elevation dataset is GTOPO30 DEM (USGS, 1996). It is re-projected onto the satellite grid by use of the re-projection routines presented in Appendix F. Reverse orthorectification would be needed to correct the elevation dataset for "view parallax" of the geostationary satellite data. The view parallax of a 4 km high mountain viewed at a 45 $^\circ$ view zenith angle yields a geographic shift of 4 km, and this corresponds to a full pixel. Since few pixels are affected by a view parallax of more than half a pixel this correction is not implemented yet.

E.2 Land-Water Mask

A land-water mask is needed in most satellite processing systems for separately carrying out cloud masks tests between land and ocean, to decrease spatial variability tests at land/water boundaries, for limiting the retrieval of physical parameters to either land or ocean or for navigation (using a coastline matching method). The water mask is used in GeoSatClim is based on the publicly available Global, Self-consistent, Hierarchical, High-resolution Shoreline (GSHHS) database (Wessel and Smith, 1996), version 2.1. The GSHHS vector data is available in a spatial resolution of up to 100 m, which allows a precise delineation of water bodies with an area of 1 km^2 or higher coherent with the maximum pixel resolution of the HRV channel on the MSG SEVIRI sensor. GSHHS includes four levels of detail: 1: ocean vs. land; 2: lake on land; 3: island on lake; 4: pond on island. Only level 1 is used in GeoSatClim and the vector-based GSHHS dataset is rendered on a regular geographic grid by setting the shoreline to 1 and ocean to 0.

E.3 Re-Analysis Data

Time-and Space-dependent re-analysis data from the ECMWF ERA Interim dataset (Berrisford et al., 2009; Dee et al., 2011) is used on a 6 hourly and 1° x 1° geographical grid.

F Geographic Projections

The following geographic projections are implemented in GeoSatClim in order to allow reading satellite input data, boundary conditions (such as NWP re-analysis data, topography or emissivity maps) and to re-project the retrieved satellite variables into a user-specified geographical output grid.

F.1 Meteosat First Generation (forward)

The forward projection formulas for the Meteosat First Generation satellites as published by EUMETSAT (2011) are used.

F.2 Meteosat First Generation (inverse)

The inverse projection formulas for the Meteosat First Generation satellites as published by EUMETSAT (2011) are used.

F.3 Meteosat Second Generation (forward)

The forward projection formulas for geostationary satellites as published by Coordination Group for Meteorological Satellites (1999) are used.

F.4 Meteosat Second Generation (inverse)

The inverse projection formulas for geostationary satellites as published by Coordination Group for Meteorological Satellites (1999) are used.

F.5 Swiss Orthographic (forward)

The approximate forward reprojection formula published by Swisstopo (2005) are used. They are appropriate for up to 1 m accuracy.

F.6 Swiss Orthographic (inverse)

The approximate inverse reprojection formula published by Swisstopo (2005) are used. They are appropriate for up to 1 m accuracy.

F.7 MODIS Sinusoidal (forward)

This projection transforms longitude λ (°E) and latitude ϕ (°N) into the MODerate resolution Imaging Spectroradiometer (MODIS) sinusoidal projection. The formulas are implemented after the tilemap3 software (Version 4.0 by Robert Wolfe, November 13, 2003):

$$x = \left(\cos\left(\phi\frac{\pi}{180}\right)\frac{\lambda}{360} + 0.5\right) n_h \cdot n_s - 0.5 \quad (122)$$

$$y = \left(\frac{-\phi}{180} + 0.5\right) n_v \cdot n_l - 0.5, \quad (123)$$

where x is the global horizontal pixel coordinate and y is the global vertical pixel coordinate. $n_h = 36$ and $n_v = 18$ are the number of horizontal and vertical tiles. Each tile has $n_s = 1200 \cdot \mathrm{res}$ samples and $n_l = 1200 \cdot \mathrm{res}$ lines, where res (km) is the MODIS sinusoidal pixel resolution (e.g. 0.25, 0.5 or 1 km). For the upper left (UL) pixel center of UL tile (MODIS: h00v00) $x = 0$ and $y = 0$. For $\lambda = -180.0$ and $\phi = 90.0$ $x = -0.5$ and $y = -0.5$. x increases from west to east and reaches 43199 for the easternmost pixel of the easternmost tile (h35vYY) with the 1 km grid. y increases from north to south and reaches 21599 for the southernmost pixel of the southernmost tile (hXXv17) with the 1 km grid.

From the MODIS global pixel coordinates The MODIS horizontal and vertical tile numbers h and v and tile sample/line numbers s and l can be calculated:

$$h = \min(\max(\mathrm{int}\left(\frac{x+0.5}{n_s}\right), 0), n_h - 1) \quad (124)$$

$$v = \min(\max(\mathrm{int}\left(\frac{y+0.5}{n_l}\right), 0), n_v - 1) \quad (125)$$

$$s = x - h \cdot n_s \quad (126)$$

$$l = y - v \cdot n_l \quad (127)$$

The horizontal and vertical tile numbers and sample/line numbers are zero-based: $h = 0..35$, $v = 0..17$, $s = 0..1200 \cdot \mathrm{res} - 1$ and $l = 0..1200 \cdot \mathrm{res} - 1$.

F.8 MODIS Sinusoidal (inverse)

This projection transforms the MODIS sinusoidal projection into longitude λ (°E) and latitude ϕ (°N). The formulas are implemented after the tilemap3 software (Version 4.0 by Robert Wolfe, November

13, 2003):

$$\phi = -(\frac{y+0.5}{n_v \cdot n_l} - 0.5) \cdot 180 \tag{128}$$

$$\lambda = \frac{(\frac{x+0.5}{n_h \cdot n_s} - 0.5) \cdot 360}{\cos\left(\phi \frac{\pi}{180}\right)}, \tag{129}$$

where the global pixel coordinates x and y can be calculated from the MODIS horizontal and vertical tile numbers h and v and tile sample/line numbers s and l:

$$x = s + h \cdot n_s \tag{130}$$

$$y = l + v \cdot n_l. \tag{131}$$

F.9 Orthographic (forward)

The orthographic projection is a commonly used map projection in cartography. It is used here to calculate north-south or west-east distances for each pixel to its neighboring pixel on either the irregular satellite grid or on the regular longitude/latitude grid. The equations to project latitude ϕ (°N; radians) and longitude λ (°E; radians) onto the x and y northing [m] and easting [m] coordinates of the tangent plane are:

$$x = R \cos\phi \sin(\lambda - \lambda_0) \tag{132}$$

$$y = R \left[\cos\phi_0 \sin\phi - \sin\phi_0 \cos\phi \cos(\lambda - \lambda_0)\right], \tag{133}$$

where ϕ_0 and λ_0 are the center latitude and longitude of the geographic domain [radians] and R is the radius [m] of the spherical earth. Orthographic projection of the ellipsoidal earth is not implemented. The potential gain in accuracy of such a transformation would not be justified for the application in “GeoSatClim ”. Areas outside of the projectable area, such as areas on the other side of the hemisphere, should not be projected. They are excluded by assuring that $\cos c = \sin\phi_0 \sin\phi + \cos\phi_0 \cos\phi \cos(\lambda - \lambda_0) \geq 0$, where c is the distance of ϕ and λ to the projection center (thus, negative distances are not allowed).

F.10 Orthographic (inverse)

The inverse orthographic projection is required to calculate longitude and latitude for orthographic coordinates, as for instance needed when calculating bilinear interpolation indices for the orthographic forward projection:

$$\phi = \arcsin\left[\cos c \sin\phi_0 + \frac{y \sin c \cos\phi_0}{\rho}\right] \quad (134)$$

$$\lambda = \lambda_0 + \arctan\left[\frac{x \sin c}{\rho \cos\phi_0 \cos c - y \sin\phi_0 \sin c}\right], \quad (135)$$

where

$$\rho = \sqrt{x^2 + y^2} \quad (136)$$

$$c = \arcsin(\rho/R), \quad (137)$$

and where the $\arctan$ formula needs to separate all four quadrants, thus the Fortran or C atan2(x,y) function with two arguments has to be used.

F.11 Rotated Pole (forward)

Rotated pole coordinates are often used in regional climate models like the COnsortium for Small-scale MOdeling (COSMO) model. The following formulas are used to project latitude ϕ (°N; radians) and longitude λ (°E; radians) onto rotated latitude ϕ_r (°N; radians) and rotated longitude λ_r (°E; radians):

$$\phi_r = \arcsin\left[\cos\phi_p \cos\phi \cos(\lambda - \lambda_p) + \sin\phi_p \sin\phi\right] \quad (138)$$

$$\lambda_r = \arctan\left[\frac{-\sin(\lambda - \lambda_p)\cos\phi}{-\sin\phi_p \cos\phi \cos(\lambda - \lambda_p) + \cos\phi_p \sin\phi}\right], \quad (139)$$

where ϕ_p and λ_p are the rotated pole latitude and longitude. The $\arctan$ formula needs to separate all four quadrants, thus the Fortran or C atan2(x,y) function with two arguments has to be used.

F.12 Rotated Pole (inverse)

The inverse formula is for instance needed to generate reverse indices for bilinear interpolation of regular to rotated pole coordinates:

$$\phi = \arcsin\left[\cos\phi_p \cos\phi \cos\lambda + \sin\phi_p \sin\phi\right] \quad (140)$$

$$\lambda = \arctan\left[\frac{\sin\lambda_p(-\sin\phi_p \cos\lambda \cos\phi + \cos\phi_p \sin\phi) - \cos\lambda_p \sin\lambda \cos\phi}{\cos\lambda_p(-\sin\phi_p \cos\lambda \cos\phi + \cos\phi_p \sin\phi) + \sin\lambda_p \sin\lambda \cos\phi}\right], \quad (141)$$

where the $\arctan$ formula needs to separate all four quadrants, thus the Fortran or C atan2(x,y) function with two arguments has to be used.

F.13 Re-Projection

Above forward and inverse projection formulas are part of a re-projection toolset specifically created for the GeoSatClim processing. The re-projection can be carried out from any regular input to any regular output grid. For instance, the regular line / column grid of the geostationary satellite projection can be reprojected onto the rotated pole longitude / latitude grid of the COSMO model by a single call to a wrapper function which carries out the following re-projection steps:

1. reprojection of input grid x_i and y_i to input grid λ_i and ϕ_i coordinates (inverse projection)
2. reprojection of input grid λ_i and ϕ_i to output x_o and y_o coordinates (forward projection)
3. reprojection of output grid x_o and y_o to output grid λ_i and ϕ_i coordinates (inverse projection)
4. reprojection of output grid λ_i and ϕ_i coordinates to input x_i and y_i coordinates (forward projection)

If input or output coordinates are already in the geographic projection, either step 1 or 3 are not needed. Based on step 2 a histogram of the number and locations of input grid points covering each grid cell of the regular output grid is calculated. Reverse indices for spatially aggregating input grid cells within the output grid cells derived from the histogram, relating each grid cells of the output grid to the matching grid cells in the input grid. Based on step 4 bilinear interpolation indices are calculated relating each output grid cell to its respective location in the regular input grid. Based on step 4 nearest neighbor interpolation indices are created as well. The reverse indices and the bilinear (BIL) and nearest neighbor (NN) interpolation indices are cached for subsequent re-projection calls within the same processing.

Depending on the type of variable a different re-projection method is chosen. Re-projection is carried out by means of bilinear interpolation if the output grid size in is less than half of the input grid size. Spatial aggregation with nearest neighbor filling is performed for upscaling. Qualitative data (e.g. land cover types) cannot be re-projected at this point. Predominant pixel sampling for such data will be implemented in the future. Other geographic projections available from common projection libraries such as “proj4” will also be accessible in the future.

G Skill Scores

G.1 Binary Skill Scores

Probability of Detection (POD), False Alarm Rate (FAR), the Hansen Kuiper’s Discriminant (HK) and the Hit Rate (HR) are formulated after Wilks (2011). $CM = 0$ corresponds to $CA \leq 1$ okta and $CM = 2$ corresponds to $CA \geq 7$ okta. The CA range of $2 - 6$ is discarded from the binary skill score calculation.

G.2 Continuous Validation Scores

The statistical quantities mean, mean bias error (MBE) and root mean square error (RMSE) of continuous states such as CFC are calculated after Wilks (2011).

G.3 The Standard Normal Homogeneity Test

The Standard Normal Homogeneity Test (SNHT) seeks for inhomogeneities in a time series. It derives a statistic $T(k)$ where changes in the standardized mean before and after each step (i.e. months in this study) are calculated. Large difference between the mean values before and after a time step indicates a possible break in a time series. Following Alexandersson (1986), statistic $T(k)$ for time step k is defined as:

$$T(k) = k\bar{z}_1^2 + (n-k)\bar{z}_2^2; k \in 1, 2, 3, \ldots, n. \tag{142}$$

The standardized means z_1^2 and $\bar{z}_2^2$ are calculated as:

$$\bar{z}_1 = \frac{1}{k}\sum_{i=1}^{k}\frac{Y_i - \bar{Y}}{\sigma}, \tag{143}$$

$$\bar{z}_2 = \frac{1}{n-k}\sum_{i=k+1}^{n}\frac{Y_i - \bar{Y}}{\sigma}, \tag{144}$$

where Y_i stands for the value at a time step i, $\bar{Y}$ for the mean, and σ for the standard deviation of the whole time series.

A large difference between the mean value before ($\bar{z}_1$) and after ($\bar{z}_2$) the time step k leads to high values of $T(k)$. Khaliq and Ouarda (2007) provided critical values of $T(k)$ depending on n which signifies a break in a time series at several confidence levels. In this report for $n = 300$ (25 years $\times$ 12 months) we employed the critical value of 10.02 for 95% of confidence level.